International Geology Review, 2013
Vol. 55, No. 11, 1418–1444, http://dx.doi.org/10.1080/00206814.2013.780722

Oxidation state of lithospheric mantle along the northeastern margin of the North China Craton: implications for geodynamic processes

Jian Wang[a]*, Keiko Hattori[b] and Zhipeng Xie[a]

[a]*College of Earth Sciences, Jilin University, Changchun, 130061, China;* [b]*Department of Earth Sciences, University of Ottawa, Ottawa, ON, Canada K1N 6N5*

(*Accepted 25 February 2013*)

Quaternary volcanic rocks in the Kuandian (KD), Longgang (LG), Changbaishan (CBS), Wangqing (WQ), and Jilin (JL) volcanic centres in eastern Liaoning and southern Jilin provinces contain mantle xenoliths of spinel-facies lherzolites and minor harzburgites. Among the study sites, the KD, LG, and CBS volcanic fields are located on the northeastern margin of the North China Craton (NCC), whereas the WQ and JL fields lie on the southern margin of the Xing'an–Mongolia Orogenic Belt (XMOB). The (Fo) components of olivine (Ol) and Cr# (=Cr/(Cr + Al)) of spinel, together with trace element abundance of clinopyroxene, suggest that the subcontinental lithospheric mantle (SCLM) in the study area has undergone a low degree (4–6%) of partial melting. The rocks do not show modal metasomatism, but clinopyroxene grains in selected samples show elevated large ion lithophile element compositions, suggesting that the mantle xenoliths underwent minor cryptic metasomatism by exchange with a silicate melt. Two-pyroxene thermometry yielded equilibration temperatures ranging from 740°C to 1210°C. The corresponding oxygen fugacity (fO_2) was calculated to range from FMQ –2.64 to +0.39 with an average of –0.59 ($n = 53$). The oxidation state is comparable to that of abyssal peridotites and the asthenospheric mantle. We failed to discover differences in equilibration temperatures and oxidation state between lherzolites and harzburgites, suggesting that partial melting did not affect fO_2 values. In addition, similar fO_2 of non-metasomatized and metasomatized samples suggest that metasomatism in the region did not affect fO_2. Our data suggest that the present SCLM beneath the northeastern margin of the NCC and the southern margin of the XMOB are very similar and likely formed from a fertile asthenosphere after delamination of an old lithospheric keel below the NCC in response to the west-dipping subduction of the Pacific oceanic plate since early to middle Mesozoic time.

Keywords: subcontinental lithospheric mantle; mineral chemistry; oxidation state (fO_2); upwelling asthenosphere; North China Craton

Introduction

Oxygen fugacity is an important parameter in controlling the physical and chemical interactions between reservoirs within the mantle and between mantle and crust (Frost and McCammon 2008). It affects metal mobility, gas species, and the nature of partial melt (Ballhaus and Frost 1994). Therefore, the study on oxidation state is important. In addition, it is closely linked to the occurrences of mineral deposits. For example, the crystallization of diamond requires highly reduced oxidation condition in the lithospheric mantle (Creighton *et al*. 2010), whereas the formation of large Cu deposits is facilitated by oxidized mantle conditions so that metals can be released from the mantle to the crust (Hattori and Keith 2001; Mungall 2002). Evaluating the redox conditions of the subcontinental lithospheric mantle (SCLM) thus contributes to understanding of the distribution of natural resources in time and space.

A significant variation is observed in fO_2 in lithospheric upper mantle, but its cause is still poorly understood. Partial melting is generally considered to result in low fO_2 in the residual mantle as Fe^{3+} is preferentially incorporated in melt (e.g. Canil *et al*. 1994). This is supported by low fO_2 in refractory peridotites beneath ancient cratons that show high Cr# (=Cr/(Cr + Al)) in spinel (Spl) and high Mg# (=Mg/(Mg + Fe)) in Ol (Woodland and Koch 2003). In contrast, a positive correlation between fO_2 and Cr# in Spl in many subarc mantle peridotites is explained by the metasomatism by oxidizing fluids from slabs (e.g. Ballhaus 1993; Parkinson and Arculus 1999; Parkinson *et al*. 2003; Arai and Ishimaru 2008). However, different metasomatic agents have varying oxidation states. For example, melts and/or fluids from asthenosphere are considered to be reduced (Ballhaus 1993; Frost and McCammon 2008). Therefore, the origin,

*Corresponding author. Email: wangjian304@jlu.edu.cn

composition, and nature of metasomatic agent(s) in different tectonic settings likely influence the oxidation state of mantle.

The North China Craton (NCC) is an Archaean craton, bounded by the late Palaeozoic Xing'an–Mongolia Orogenic Belt (XMOB) to the north, the early Palaeozoic Qinling Orogenic Belt to the southwest, and the Mesozoic Dabie–Sulu Ultrahigh Pressure (UHP) metamorphic belts to the south and east (e.g. Xiao *et al*. 2003) (Figure 1A). The XMOB is composed of several micro-continental blocks and/or terranes formed on the northern margin of the NCC during southward subduction of the Palaeo-Asian oceanic plate and the subsequent collision with the Siberia Craton, during the early Palaeozoic to Triassic (e.g. Xiao *et al*. 2003; Wu *et al*. 2011).

The NCC consists of two Archaean Blocks, the Eastern and Western, separated by the Trans-North China Orogen, a Palaeoproterozoic collisional belt (Figure 1A) (Wilde and Zhao 2005; Zhao *et al*. 2005; Zhang *et al*. 2006, 2007). Unlike other Archaean cratons in the world, such as the Kaapvaal Craton in South Africa and the Slave Province of the Canadian shield, the Eastern Block (EB) of NCC is underlain by a thin (<80 km) SCLM (Fan *et al*. 2000; Kusky *et al*. 2007) because the 'keel' of a thick (over 200 km), cold, and refractory lithosphere was replaced by hot, fertile asthenospheric material in Mesozoic time (Griffin and O'Reilly 2007). Most information related to the SCLM of the NCC was obtained from mantle xenoliths enclosed in Palaeozoic kimberlites, Mesozoic high-Mg diorites, and Cenozoic basalts at locations close to the marginal areas. Examples include the Xinyang, Nushan, and Xuzhou-Huainan areas on the southeastern margin, the western Shandong area (e.g. Feixian, Fangcheng, Mengyin, Shanwang, Laiwu, Hebi, Zibo, and Fuxian) on the east-central margin, and the Fuxin and Hannuoba area on the northern margin (Figure 1A). On the other hand, studies of the northeastern margin of NCC are scarce, although it is an equally important location that is close to XMOB and the subducting Pacific oceanic plate.

Previous studies on the oxidation state of the SCLM mainly focused on those underlying the Kaapvaal (Daniels and Gurney 1991; McCammon *et al*. 2001; Woodland and Koch 2003), Slave (e.g. McCammon and Kopylova 2004), and Siberian (Ionov and Wood 1992) cratons. The SCLMs below these cratons remain stable after their formation in Archaean time, whereas the SCLM below NCC has undergone substantial change in Mesozoic time. Studies conducted by Li and Wang (2002) and Wang *et al*. (2012a,b)

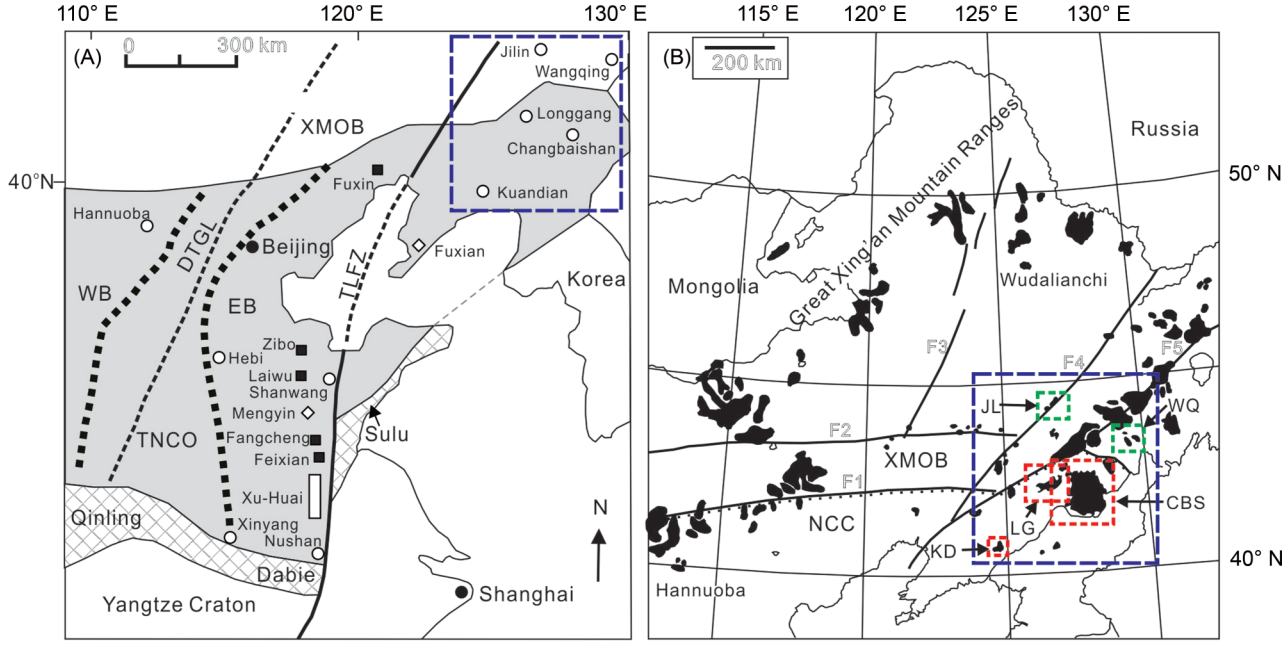

Figure 1. (A) Map of the North China Craton (NCC) showing the study area (thick dashed blue lines), the locations of the late Mesozoic high-Mg basalts and diorites of Fuxin, Zibo, Laiwu, Fangcheng, Feixian, and Xu-Huai (solid squares), early Palaeozoic diamondiferous kimberlites of Mengyin and Fuxian (open diamonds), and Cenozoic basalts (open circles). The NCC is divided by faults (thick dashed lines) into the EB, Trans-North China Orogen (TNCO), and Western Block (WB). Thin dashed lines are the Daxinganling–Taihangshan Gravity Lineament (DTGL) and Tan-Lu Fault Zone (TLFZ), respectively. The map was modified after Zhao *et al*. (2005). (B) Map of the study area showing the locations of studied Cenozoic volcanic fields and their relative positions to XMOB, major fault zones, and other Cenozoic volcanic fields (e.g. Wudalianchi and Hannuoba). KD, CBS, and LG marked with red-dashed squares are located in the northeastern margin of NCC, and WQ and JL marked with green dashed squares are located in the southern margin of XMOB (modified after Liu *et al*. 2001a). F1, Chifeng–Kaiyuan Fault Zone; F2, Xilamulun Fault Zone; F3, Nenjiang Fault Zone; F4,Yilan–Yitong Fault Zone; F5, Dunhua–Mishan Fault Zone. Cenozoic volcanoes are shown as dark-shaded areas.

represent the only systematic work on the oxidation state of SCLM underlying NCC so far. This paper reports bulk-rock and mineral compositions as well as oxidation states of SCLM based on mantle xenoliths brought by Cenozoic volcanic rocks on the northeastern margin of the NCC and the southern margin of the XMOB and discusses the origin and evolution of the SCLM in the area.

Study area and sample description

The study area, including Cenozoic volcanic fields of Kuandian (KD), Longgang (LG), and Changbaishan (CBS), is located in the eastern Liaoning and southeastern Jilin (JL) provinces. It is on the northeastern margin of NCC, approximately 100–200 km southeast of the NE-trending Dunhua–Mishan Fault Zone (F5; Figures 1A and 1B). All xenolith samples were collected during the field work in the summer of 2009 and 2010.

The KD volcanic field is composed of over 20 scoria cones and calderas, and their eruption ages are younger than 0.2 Ma (Lu *et al*. 1983). Our samples of mantle xenoliths were collected from alkali basalts of Huangyishan (HYS) and Qingyishan (QYS) volcanos, and from pyroclastic rocks of Dachuantou (DCT) volcano (Figure 1). The LG volcanic field is composed of many calderas, maars, and scoria cones, all of which formed since the Oligocene and contain lavas and pyroclastic rocks of alkali basaltic composition. Among them, Dalongwan (DLW) and Longquanlongwan (LQL) are mid-Pleistocene large maars surrounded by pyroclastic rocks, and Dayizishan (DYS) is an early to middle Pleistocene scoria cone composed mainly of alkali basaltic rocks. Mantle xenoliths were collected from pyroclastic rocks and lavas of the above three volcanoes. The CBS volcanic centre, ~150 km east of the LG volcanic field (Figure 1), is the most important volcano in China and North Korea because of its magnitude, long eruption history, and frequent violent eruptions (Wei *et al*. 2007; Kuritani *et al.* 2009). An early stage of basaltic shield formation in a short period of 2.77–0.31 Ma was followed by trachytic pyroclastic eruptions to form cones and later by ignimbrite formation (Wang *et al*. 2003; Wei *et al*. 2007). The studied mantle xenoliths were collected from the trachybasalt of the shield-forming stage in a nature forest park of Hongsongwang, ~50 km north to the Tianchi crater lake (Figure 1). For comparison, we also collected mantle xenoliths from the Cenozoic Pingfengshan volcano of the Wangqing (WQ) volcanic field and the Qiantuanshan and Houtuanshan volcanoes of the Cenozoic JL volcanic field, which are located in the southern margin of the XMOB (Figure 1) and composed mainly of Ol-bearing alkali basaltic rocks.

Xenoliths are Spl-facies litherzolites and harzburgites in the KD, LG, CBS, and JL volcanic fields (Figures 2A and B). We examined a total of 55 samples of mantle xenoliths: 19 from KD; 19 from LG; 8 from CBS; 5 from WQ; and 4 from JL. The samples range in size from 10 to 50 cm in the longest dimension. They are rounded, unaltered, and show no evidence of weathering and/or serpentinization, but the rims of several samples show evidence of interaction with host basaltic magmas. These parts were removed before preparing samples for bulk rock analysis. The xenoliths are further divided into two subtypes based on the mineral mode in thin sections: lherzolites ($n = 45$) and harzburgites ($n = 10$). All harzburgites are from LG. Lherzolite shows protogranular or porphyroclastic textures (2–5 mm in grain size; Figures 2C and D) and is composed of Ol (50–70 vol.%), orthopyroxene (Opx, 15–30 vol.%), clinopyroxene (Cpx, 5–15 vol.%), and Spl (~5 vol.%). Harzburgite shows porphyroblastic to equigranular textures (~2–3 mm in grain size; Figure 2E) with mineral assemblage of Ol (55–85 vol.%), Opx (10–25 vol.%), Cpx (<10 vol.%), and Spl (<5 vol.%). Several samples contain thin veins of basalts (<1 cm in width) cutting through peridotites. Hydrous minerals (phlogopite and amphibole) are not found in the studied xenoliths, but they are reported in mantle xenoliths from other LG volcanoes by other workers (e.g. Shi *et al*. 1999).

Pyroxenite xenoliths are rare and found only in the KD and WQ volcanic fields. They are Ol-bearing websterites and/or orthopyroxenites with equigranular textures (Figure 2F). Pyroxenite xenoliths are not studied because this study focuses on the oxidation state of mantle peridotites.

Analytical method

Mineral compositions were determined by a JEOL (JXA-8100, Tokyo, Japan) microprobe at China University of Geosciences in Wuhan using 15 kV accelerating voltage, 20 nA beam current, focused beam size (<1 μm), and natural and synthetic mineral standards. A counting time of 20 s was used for all elements except 50 s for Ca and Ni in Ol. The contents of Fe^{3+} in Spl are calculated assuming Spl stoichiometry. Compositions for a specific mineral in individual samples show a narrow range. Therefore, only representative mineral compositions are listed in Table 1. Trace element compositions of Cpx were analysed using an excimer laser ablation inductively coupled plasma mass spectrometer (LA-ICP-MS) at the State Key Laboratory of Geological Processes and Mineral Resources, China University of Geosciences in Wuhan. The analytical procedure is the same as that described in Liu *et al.* (2001b). The analysis of US Geological Survey basalt glass standards BCR-2G and BHVO-2G suggests the precision and accuracy to be better than 7%.

Major and minor elements of bulk rocks were determined using a Philips PW 2400 X-ray fluorescence spectrometer after fusing the sample powder with $LiBO_3$ at the University of Ottawa. Precision based on replicate runs

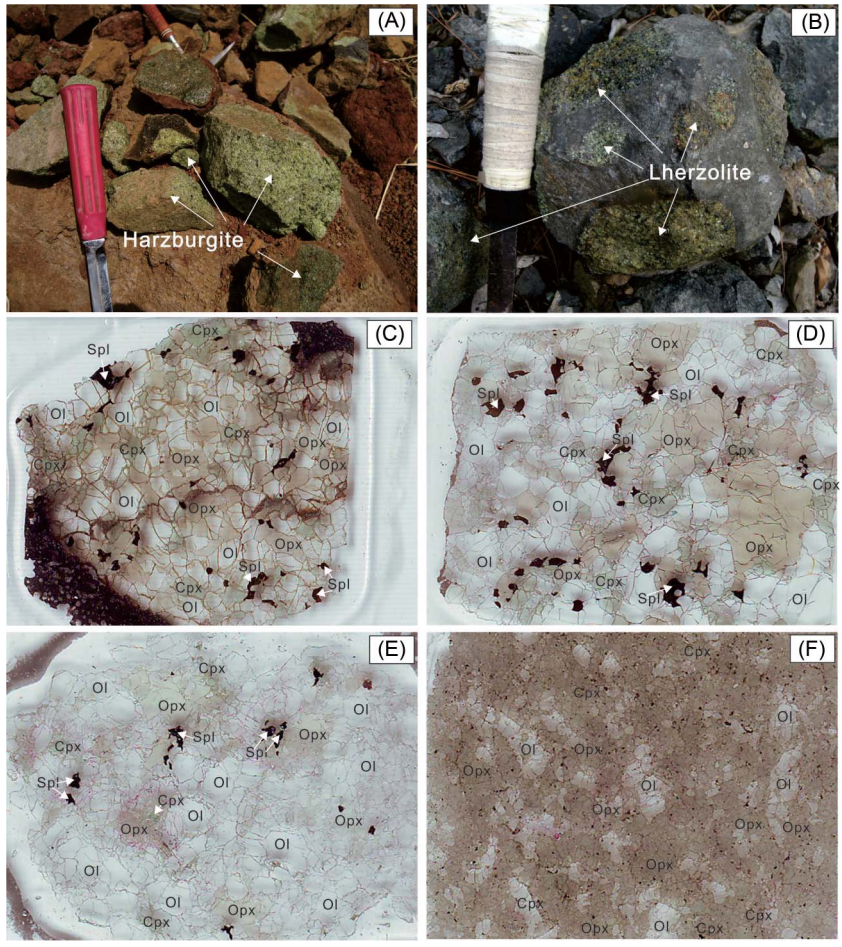

Figure 2. (A) Field photograph of a harzburgite sample (DYS7) from the LG volcanic field. (B) Field photograph of a lherzolite sample (HSW4) from the CBS volcanic field. (C) Photograph of a lherzolite (HYS26) from the KD volcanic field. (D) Photograph of a lherzolite (HSW4) from the CBS volcanic field. (E) Photograph of a harzburgite (DYS7) from the LG volcanic field. (F) Photograph of an Ol-bearing websterite (PFS4) from the WQ volcanic field.

of 11 samples is ±0.35% for Al_2O_3, ± 0.48% for MgO, ±1.3% for Cr, and ±9.2% for Ni. The accuracy, which was monitored using references of MRG-1 and Sy-2, shows ±0.039% for Al_2O_3, 0.28% for MgO, 3.4% for Cr, and 4.0% for Ni. Precision and accuracy are less than 1% and 10% for other major and minor elements.

Mineral chemistry and bulk rock composition

Mineral chemistry

Olivine

Ol grains in lherzolite from KD, LG, and CBS show Fo (=100 × Mg/(Mg + Fe)) values ranging from 88.2 to 91.0, similar to Fo (88.8–90.9) of the lherzolite from WQ and JL (Table 1). The average Fo value for lherzolites in the study area is 89.6, lower than that (90.4) of harzburgites (Table 1). The data are consistent with the interpretation that harzburgite has undergone higher degrees of partial melting (more refractory) than lherzolite. The contents of NiO (=0.36–0.45 wt.%) are similar in all lherzolite and harzburgite samples, which are identical to values (0.36–0.45 wt.%) of Ol from Shanwang mantle xenoliths reported by Zheng *et al*. (2006). Different grains of Ol and cores and rims of grains have similar composition in individual samples of the study area, suggesting that Ol has attained equilibration. An exception is CaO, which is higher in the rim (<10 μm in thickness) than in the core of several samples. The evidence suggests that Ca in Ol is affected by host basaltic melt.

Orthopyroxene

The values of Mg# (= Mg/(Mg + total Fe)) of Opx are similar among lherzolite samples from KD + LG + CBS (0.891–0.921) and WQ + JL (0.896–0.912) (Table 1). Their average Mg#, 0.905, in lherzolites is slightly lower than that in LG harzburgite samples (0.912). The Mg# of Opx are always higher than Fo of coexisting Ol in

Table 1. Representative compositions of minerals in peridotites from the Cenozoic volcanic fields in the northeast margin of NCC and southern margin of XMOB.

Volcanic field	Longgang																		
Sample lithology	DLW1 Harz	DLW3 Lher	DLW5 Lher	DLW6 Harz	DLW8 Lher	DYS1 Harz	DYS4 Lher	DYS5 Harz	DYS7 Harz	DYS9 Lher	DYS12 Harz	DYS13 Harz	DYS14 Harz	LQL1 Harz	LQL3 Lher	LQL4 Lher	LQL6 Lher	LQL7 Harz	LQL8 Lher
Olivine																			
SiO_2	41.32	40.87	41.05	41.21	40.57	41.16	40.80	41.14	41.30	41.38	41.83	41.39	41.17	40.64	41.20	40.50	35.21	40.30	40.34
Al_2O_3	0.04	0.04	0.04	0.05	0.05	0.07	0.07	0.06	0.06	0.05	0.02	0.06	0.03	0.06	0.04	0.08	0.11	0.05	0.49
FeO	9.16	10.12	10.14	8.94	10.43	8.94	10.46	9.02	8.98	10.03	9.06	8.91	8.89	9.71	9.85	10.02	9.33	10.73	10.59
MnO	0.12	0.16	0.15	0.12	0.11	0.14	0.10	0.14	0.09	0.10	0.11	0.12	0.12	0.12	0.11	0.13	0.12	0.15	0.15
MgO	48.55	47.56	48.25	48.92	48.36	48.98	47.94	49.12	48.68	47.24	48.75	48.65	49.46	48.46	48.13	48.73	45.49	48.01	47.42
CaO	0.13	0.14	0.15	0.09	0.03	0.10	0.10	0.08	0.06	bd	0.06	0.08	0.02	0.11	0.03	0.11	0.20	0.06	0.13
NiO	0.43	0.39	0.42	0.43	0.41	0.39	0.36	0.36	0.39	0.41	0.44	0.39	0.43	0.41	0.40	0.37	0.37	0.42	0.40
Total	99.86	99.48	100.2	99.77	99.99	99.78	99.89	99.95	99.60	99.29	100.3	99.65	100.2	99.56	99.81	99.94	90.90	99.76	99.62
Mg#[b]	0.904	0.893	0.895	0.907	0.892	0.907	0.891	0.907	0.906	0.894	0.906	0.907	0.908	0.899	0.897	0.897	0.90	0.889	0.889
Orthopyroxene																			
SiO_2	55.88	54.73	56.03	56.95	55.60	56.13	55.22	56.09	56.49	54.90	56.44	56.59	55.72	54.45	55.96	55.43	53.87	54.39	53.59
TiO_2	0.15	0.09	0.07	0.08	0.07	0.11	0.11	0.13	0.10	0.14	0.13	0.13	0.13	0.10	0.12	0.09	0.11	0.15	0.14
Al_2O_3	2.82	4.14	3.55	2.52	3.29	2.81	4.14	2.85	2.78	3.61	2.71	2.91	2.78	3.27	3.08	3.88	4.32	3.60	4.57
Cr_2O_3	0.58	0.41	0.30	0.40	0.21	0.45	0.28	0.49	0.44	0.24	0.42	0.48	0.42	0.53	0.24	0.46	0.34	0.44	0.34
FeO	5.52	6.42	6.31	5.70	6.67	5.69	6.72	5.71	5.61	6.32	5.80	5.65	5.63	5.94	6.32	6.50	6.01	6.68	6.73
MnO	0.10	0.16	0.18	0.14	0.13	0.10	0.17	0.13	0.11	0.14	0.12	0.10	0.10	0.12	0.14	0.12	0.14	0.15	0.15
MgO	33.83	32.70	32.52	33.42	33.18	33.75	32.23	33.23	32.98	33.74	33.33	32.97	34.46	33.66	33.31	32.34	33.45	33.65	33.08
CaO	0.77	0.64	0.60	0.49	0.40	0.62	0.54	0.71	0.63	0.50	0.53	0.70	0.57	0.87	0.47	0.84	0.74	0.76	0.88
NiO	0.12	0.13	0.15	0.15	0.09	0.16	0.15	0.11	0.09	0.13	0.11	0.14	0.13	0.12	0.12	0.11	0.14	0.12	0.14
Na_2O	0.09	0.09	0.12	0.10	0.04	0.10	0.07	0.13	0.09	0.07	0.06	0.12	0.06	0.08	0.04	0.13	0.13	0.09	0.10
Total	99.88	99.51	99.83	99.95	99.66	99.92	99.62	99.59	99.31	99.81	99.64	99.80	99.99	99.13	99.80	99.92	99.25	100.0	99.73
Mg#[b]	0.916	0.901	0.902	0.913	0.899	0.914	0.895	0.912	0.913	0.905	0.911	0.912	0.916	0.910	0.904	0.899	0.91	0.900	0.898
Clinopyroxene																			
SiO_2	50.78	51.54	51.77	52.63	51.82	52.13	51.68	52.15	52.53	51.29	52.58	51.95	51.75	51.92	50.97	52.29	51.42	51.39	51.55
TiO_2	0.93	0.53	0.37	0.43	0.46	0.40	0.41	0.43	0.39	0.56	0.51	0.43	0.54	0.22	0.54	0.31	0.31	0.53	0.39
Al_2O_3	4.46	6.46	5.47	4.41	6.18	4.42	5.66	4.53	4.37	6.10	4.67	4.90	5.32	4.10	5.63	4.84	5.96	4.71	5.43
Cr_2O_3	1.89	0.64	0.98	1.60	0.71	1.34	0.70	1.37	1.20	0.71	1.41	1.17	1.66	0.92	0.99	0.80	0.72	0.92	0.56
FeO(t)[a]	3.09	2.74	3.01	2.35	2.53	2.54	2.84	2.67	2.52	2.71	2.45	2.75	2.37	3.05	2.60	2.87	2.76	3.12	3.18
MnO	0.13	0.05	0.09	0.11	0.05	0.03	0.08	0.07	0.07	0.10	0.04	0.07	0.04	0.06	0.04	0.08	0.06	0.06	0.08
MgO	17.31	14.97	16.10	15.83	15.13	16.23	15.89	16.61	16.10	15.23	15.97	16.63	15.22	17.58	15.21	16.53	16.29	16.30	16.48
CaO	20.62	20.79	20.50	20.80	21.48	20.87	21.55	20.45	20.94	21.20	20.78	19.93	20.46	20.59	21.13	20.63	19.99	20.94	20.24
NiO	0.09	0.08	0.08	0.08	0.09	0.06	0.07	0.10	0.09	0.06	0.06	0.09	0.08	0.07	0.06	0.08	0.07	0.08	0.08
Na_2O	0.43	1.59	1.32	1.42	1.56	1.36	1.22	1.33	1.44	1.63	1.52	1.51	1.91	0.93	1.57	1.10	1.50	1.23	1.33
Total	99.72	99.38	99.71	99.66	100.0	99.39	100.1	99.71	99.64	99.61	99.99	99.44	99.36	99.45	98.73	99.52	99.08	99.28	99.33
Mg#[b]	0.909	0.907	0.905	0.923	0.914	0.919	0.909	0.917	0.919	0.909	0.921	0.915	0.920	0.911	0.913	0.911	0.91	0.903	0.902
Cr#[c]	0.222	0.062	0.107	0.195	0.072	0.169	0.077	0.169	0.156	0.073	0.169	0.138	0.173	0.131	0.106	0.100	0.075	0.116	0.065
Spinel																			
SiO_2	0.14	0.09	0.14	0.07	0.05	0.07	0.11	0.10	0.10	0.07	0.07	0.10	0.07	0.13	0.09	0.11	0.06	0.04	0.16
TiO_2	0.73	0.11	0.17	0.20	0.07	0.36	0.32	0.37	0.37	0.10	0.32	0.36	0.22	0.19	0.10	0.17	0.10	0.28	0.21
Al_2O_3	36.79	57.09	53.49	41.39	56.69	40.51	56.18	39.82	39.27	57.52	39.22	40.72	41.23	42.92	53.69	49.91	55.62	47.00	55.65
Cr_2O_3	30.19	9.45	13.21	26.53	10.30	27.19	9.54	27.51	27.87	9.86	28.64	27.33	26.52	24.07	13.99	16.80	12.10	19.39	10.02
FeO(t)[a]	13.12	11.06	11.83	12.29	10.97	12.52	12.29	12.55	12.71	11.10	13.37	12.35	12.75	12.80	11.30	12.36	10.53	14.19	12.36
MnO	0.21	0.14	0.11	0.17	0.12	0.18	0.09	0.14	0.15	0.12	0.20	0.17	0.13	0.18	0.10	0.14	0.08	0.13	0.11
MgO	18.18	20.97	20.18	18.93	20.92	18.72	20.57	18.82	18.82	20.61	17.77	18.56	18.42	18.49	19.64	19.99	20.32	18.63	21.02
NiO	0.34	0.38	0.43	0.33	0.43	0.32	0.43	0.29	0.31	0.42	0.33	0.31	0.30	0.31	0.35	0.35	0.36	0.33	0.39
Total	99.73	99.29	99.59	99.94	99.56	99.87	99.56	99.61	99.61	99.85	99.94	99.96	99.63	99.13	99.27	99.84	99.16	99.99	99.93
Mg#[b]	0.759	0.815	0.794	0.782	0.815	0.774	0.799	0.779	0.781	0.799	0.743	0.767	0.763	0.765	0.778	0.796	0.797	0.753	0.813
Cr#[c]	0.355	0.100	0.142	0.301	0.109	0.310	0.102	0.317	0.322	0.103	0.329	0.310	0.302	0.273	0.149	0.184	0.127	0.217	0.108

(*Continued*)

Table 1. (Continued).

Volcanic field	Kuandian																		
Sample lithology	DCT1 Lher	DCT2 Lher	DCT3 Lher	DCT5 Lher	DCT8 Lher	DCT9 Lher	HYS1 Lher	HYS4 Lher	HYS2 Lher	HYS7 Lher	HYS13 Lher	HYS14 Lher	HYS24 Lher	HYS26 Lher	QYS8 Lher	QYS10 Lher	QYS14 Lher	QYS15 Lher	QYS18 Lher
Olivine																			
SiO_2	38.42	40.72	40.18	38.24	39.14	38.74	38.93	38.51	38.85	38.85	38.78	38.43	38.47	39.29	38.20	40.94	41.21	40.77	40.64
Al_2O_3	0.03	0.02	0.04	0.09	0.02	0.08	0.05	0.02	0.03	0.04	0.08	0.08	0.02	0.04	0.04	0.05	0.05	0.06	0.05
FeO	11.09	9.07	9.23	9.73	9.42	10.31	10.33	10.80	10.18	10.96	10.29	9.22	9.43	11.45	9.13	10.32	10.06	10.06	11.08
MnO	0.11	0.08	0.11	0.13	0.10	0.06	0.11	0.10	0.08	0.13	0.14	0.11	0.16	0.14	0.11	0.11	0.09	0.14	0.14
MgO	49.28	49.37	49.42	50.94	49.93	49.53	49.28	49.33	49.73	49.08	49.26	50.92	50.77	48.01	51.41	47.85	48.05	48.24	47.49
CaO	0.04	0.03	0.02	0.13	0.05	0.07	0.01	0.02	0.02	0.01	0.16	0.03	0.12	0.07	0.06	0.00	0.06	0.11	0.06
NiO	0.36	0.39	0.42	0.35	0.43	0.42	0.40	0.42	0.44	0.43	0.37	0.41	0.40	0.39	0.39	0.41	0.42	0.39	0.35
Total	99.35	99.71	99.44	99.63	99.10	99.27	99.15	99.21	99.36	99.51	99.12	99.21	99.40	99.42	99.36	99.71	99.98	99.77	99.82
Mg#[b]	0.89	0.91	0.91	0.90	0.90	0.90	0.89	0.89	0.90	0.89	0.89	0.91	0.91	0.88	0.91	0.89	0.90	0.90	0.88
Orthopyroxene																			
SiO_2	53.53	56.3	54.31	52.68	53.36	52.73	53.94	53.46	54.16	53.91	52.06	54.94	54.02	53.63	53.82	55.27	55.62	55.29	55.15
TiO_2	0.16	0.1	0.08	0.19	0.13	0.15	0.1	0.13	0.12	0.11	0.14	0.06	0.14	0.16	0.31	0.13	0.32	0.17	0.07
Al_2O_3	3.26	2.78	3.55	5.52	4.24	5.26	3.6	4	3.19	3.1	6.17	3.39	3.65	4.69	4.15	3.45	4.15	4.64	4.54
Cr_2O_3	0.55	0.33	0.42	0.43	0.35	0.59	0.19	0.25	0.26	0.17	0.62	0.36	0.35	0.3	0.47	0.24	0.42	0.54	0.43
FeO	7.08	5.95	5.34	6.15	5.71	5.99	6.23	6.53	6.07	6.56	5.88	6.06	6.1	6.31	5.94	5.88	6.42	6.42	6.8
MnO	0.16	0.1	0.13	0.15	0.12	0.12	0.15	0.15	0.12	0.14	0.11	0.15	0.13	0.14	0.14	0.12	0.15	0.14	0.13
MgO	33.7	33.63	34.99	32.7	34.36	33.15	34.41	34.24	34.89	34.53	32.38	34.25	34.31	33.23	33.64	34.03	31.89	31.58	31.38
CaO	0.67	0.41	0.44	1.12	0.68	1.17	0.45	0.44	0.39	0.38	1.42	0.52	0.49	0.68	0.68	0.49	0.67	0.86	0.86
NiO	0.1	0.11	0.14	0.12	0.13	0.13	0.14	0.13	0.12	0.12	0.13	0.12	0.11	0.12	0.13	0.09	0.12	0.15	0.13
Na_2O	0.11	0.05	0.21	0.19	0.12	0.18	0.03	0.06	0.05	0.03	0.22	0.06	0.08	0.08	0.15	0.06	0.06	0.17	0.13
Total	99.32	99.76	99.61	99.25	99.2	99.47	99.24	99.39	99.37	99.05	99.13	99.91	99.38	99.34	99.43	99.76	99.82	99.96	99.62
Mg#[b]	0.89	0.91	0.92	0.90	0.91	0.91	0.91	0.90	0.91	0.90	0.91	0.91	0.91	0.90	0.91	0.91	0.90	0.90	0.89
Clinopyroxene																			
SiO_2	51.87	52.09	52.47	50.68	51.05	49.97	51.35	51.36	50.84	51.60	50.36	51.70	51.57	50.36	50.55	53.05	51.12	51.79	52.23
TiO_2	0.45	0.38	0.37	0.57	0.47	0.51	0.50	0.53	0.56	0.51	0.33	0.19	0.51	0.66	1.25	0.69	1.20	0.55	0.23
Al_2O_3	5.36	5.22	5.20	7.32	5.98	6.87	5.91	5.41	6.05	5.41	7.33	5.12	5.41	4.97	6.01	6.79	6.24	6.30	5.53
Cr_2O_3	1.28	1.18	1.06	0.74	0.81	1.03	0.63	0.52	0.94	0.52	0.96	1.13	0.77	0.73	0.86	0.81	0.87	1.03	0.78
FeO(t)[a]	3.44	2.16	2.11	3.16	2.54	3.24	2.35	2.46	2.42	2.53	3.64	2.56	2.25	3.02	2.64	2.24	2.62	2.82	2.85
MnO	0.10	0.05	0.05	0.05	0.08	0.09	0.05	0.07	0.06	0.04	0.08	0.07	0.05	0.11	0.05	0.04	0.05	0.06	0.08
MgO	15.02	16.24	15.68	16.38	16.21	16.64	15.54	15.68	15.40	15.56	17.85	15.86	15.49	17.35	16.03	14.07	15.91	16.05	16.38
CaO	19.68	21.01	21.32	18.29	20.38	18.21	21.12	21.66	21.03	21.37	17.23	20.94	21.74	21.46	20.61	20.39	20.57	18.73	20.11
NiO	0.10	0.09	0.07	0.08	0.09	0.06	0.08	0.07	0.10	0.09	0.08	0.07	0.08	0.08	0.09	0.07	0.10	0.10	0.08
Na_2O	2.15	1.51	1.45	1.78	1.59	1.67	1.87	1.62	1.79	1.75	1.54	1.58	1.53	0.50	1.36	1.84	1.29	1.71	1.31
Total	99.46	99.93	99.77	99.06	99.20	98.29	99.38	99.39	99.19	99.38	99.39	99.22	99.39	99.23	99.43	99.97	99.97	99.14	99.57
Mg#[b]	0.89	0.93	0.93	0.90	0.92	0.90	0.92	0.92	0.92	0.92	0.90	0.92	0.93	0.91	0.92	0.92	0.92	0.91	0.91
Cr#[c]	0.138	0.132	0.120	0.064	0.084	0.092	0.067	0.060	0.094	0.060	0.081	0.129	0.088	0.090	0.087	0.074	0.085	0.099	0.086
Spinel																			
SiO_2	0.03	0.05	0.01	0.09	0.07	0.11	0.01	0.04	0.02	0.01	0.13	0.05		0.05	0.05	0.09	0.03	0.21	0.08
TiO_2	0.35	0.11	0.10	0.23	0.16	0.29	0.10	0.09	0.08	0.10	0.32	0.06		0.17	0.49	0.10	0.48	0.28	0.13
Al_2O_3	41.05	50.95	53.60	57.54	56.02	52.07	59.38	58.87	56.76	58.22	53.38	50.43		59.17	52.08	58.48	54.21	51.28	54.68
Cr_2O_3	23.99	17.73	14.82	9.34	11.75	14.62	8.36	8.62	11.58	8.76	12.48	18.23		8.12	14.91	10.01	14.16	15.64	12.91
FeO(t)[a]	17.47	10.94	10.48	10.25	9.57	10.96	10.05	11.06	10.35	11.27	13.94	11.26		10.23	13.55	10.33	11.16	11.27	11.39
MnO	0.16	0.11	0.12	0.08	0.09	0.10	0.08	0.07	0.11	0.10	0.13	0.15		0.04	0.16	0.08	0.11	0.16	0.13
MgO	16.33	19.81	20.08	21.72	20.93	20.74	20.81	20.02	20.50	20.98	19.18	19.71		21.19	18.79	20.46	19.83	19.77	20.34
NiO	0.31	0.34	0.34	0.38	0.39	0.51	0.41	0.38	0.33	0.41	0.34	0.34		0.39	0.33	0.40	0.35	0.42	0.32
Total	99.68	100.0	99.55	99.61	98.96	99.41	99.19	99.15	99.73	99.85	99.90	100.2		99.34	100.4	99.95	100.3	99.02	99.97
Mg#[b]	0.684	0.788	0.793	0.835	0.817	0.818	0.806	0.779	0.798	0.810	0.754	0.785		0.815	0.741	0.790	0.772	0.787	0.795
Cr#[c]	0.282	0.189	0.156	0.098	0.123	0.159	0.086	0.090	0.120	0.092	0.135	0.195		0.084	0.161	0.103	0.149	0.170	0.137

(*Continued*)

Table 1. (Continued).

Volcanic field	WQ					JL			
Sample	PFS5	PFS10	PFS13	PFS15	PFS16	QTS5	QTS8	HTS6	HTS9
Lithology	Lher	Lher	Lher	Lher	Lher	Lher	Lher	Lher	Lher
Olivine									
SiO_2	38.78	40.58	40.88	38.88	39.30	38.89	38.73	38.89	37.67
Al_2O_3	0.04	0.02	0.03	0.05	0.05	0.06	0.04	0.05	0.05
FeO	9.59	10.78	10.08	9.07	10.35	10.26	10.83	10.00	9.66
MnO	0.14	0.15	0.15	0.11	0.12	0.10	0.14	0.10	0.15
MgO	50.54	47.95	48.26	50.83	48.85	49.45	48.84	49.56	51.20
CaO	0.03	0.04	0.06	0.04	0.04	0.10	0.06	0.03	0.16
NiO	0.38	0.41	0.41	0.43	0.42	0.42	0.40	0.46	0.40
Total	99.53	99.94	99.87	99.43	99.13	99.37	99.08	99.10	99.33
Mg#[b]	0.90	0.89	0.90	0.91	0.89	0.90	0.89	0.90	0.90
Orthopyroxene									
SiO_2	55.52	55.52	55.56	55.17	54.31	53.09	53.93	54.21	53.2
TiO_2	0.06	0.14	0.11	0.11	0.11	0.14	0.15	0.06	0.14
Al_2O_3	3	3.21	3.37	3.21	4.03	4.78	3.99	3.56	4.49
Cr_2O_3	0.2	0.28	0.31	0.25	0.27	0.35	0.24	0.36	0.33
FeO	5.94	6.85	6.27	5.9	5.92	6.04	6.32	5.83	6.16
MnO	0.13	0.13	0.11	0.13	0.09	0.12	0.14	0.12	0.13
MgO	33.79	33.10	33.13	34.11	34.02	33.72	33.84	34.35	33.7
CaO	0.54	0.40	0.46	0.41	0.46	0.79	0.53	0.57	0.74
NiO	0.1	0.11	0.14	0.12	0.11	0.15	0.13	0.1	0.14
Na_2O	0.12	0.09	0.13	0.09	0.04	0.12	0.07	0.06	0.12
Total	99.4	99.83	99.59	99.5	99.36	99.3	99.34	99.22	99.15
Mg#[b]	0.91	0.90	0.90	0.91	0.91	0.91	0.91	0.91	0.91
Clinopyroxene									
SiO_2	51.44	52.16	52.88	52.48	51.29	50.47	51.35	51.69	50.80
TiO_2	0.43	0.52	0.40	0.34	0.46	0.44	0.62	0.14	0.51
Al_2O_3	3.82	6.12	6.10	5.41	5.93	6.19	5.95	3.97	5.99
Cr_2O_3	1.11	1.01	1.01	0.80	0.78	0.71	0.58	0.67	0.54
FeO(t)[a]	2.55	2.51	2.27	2.20	2.32	2.98	2.67	2.48	2.84
MnO	0.09	0.06	0.03	0.07	0.06	0.07	0.07	0.07	0.05
MgO	16.59	14.60	14.40	15.49	15.48	16.47	15.56	17.10	16.04
CaO	22.65	20.94	20.51	20.94	21.37	20.42	20.68	22.06	20.79
NiO	0.06	0.09	0.07	0.08	0.09	0.09	0.07	0.10	0.08
Na_2O	0.56	1.88	2.07	1.63	1.39	1.36	1.79	0.90	1.59
Total	99.30	99.89	99.73	99.43	99.16	99.20	99.33	99.16	99.22
Mg#[b]	0.92	0.91	0.92	0.93	0.92	0.91	0.91	0.92	0.91
Cr#[c]	0.163	0.100	0.099	0.091	0.082	0.072	0.061	0.102	0.057
Spinel									
SiO_2	0.03	0.07	0.05	0.05	0.04	0.09		0.05	0.06
TiO_2	0.03	0.05	0.05	0.07	0.09	0.22		0.07	0.14
Al_2O_3	55.01	55.20	54.93	56.96	58.20	55.87		51.25	58.00
Cr_2O_3	12.13	12.51	12.47	11.49	9.43	10.97		16.06	9.01
FeO(t)[a]	12.47	11.21	10.81	9.65	9.56	11.00		11.43	10.45
MnO	0.14	0.11	0.11	0.10	0.11	0.09		0.12	0.10
MgO	19.40	20.30	20.79	20.95	21.41	21.05		19.78	21.04
NiO	0.38	0.37	0.40	0.40	0.39	0.39		0.40	0.40
Total	99.59	99.81	99.60	99.66	99.23	99.68		99.16	99.19
Mg#[b]	0.766	0.79	0.81	0.814	0.829	0.816		0.772	0.815
Cr#[c]	0.129	0.13	0.13	0.119	0.098	0.116		0.174	0.094

Notes: nd, not determined.
[a] Total Fe as FeO.
[b] $Mg\# = Mg/(Mg + Fe^{2+})$. Fe in olivine and pyroxene is assumed to be Fe^{2+}.
[c] $Cr\# = Cr/(Cr + Al)$.

each sample in the study area, which is consistent with equilibrium Fe-Mg exchange between these two phases as observed in other mantle xenoliths (e.g. Qi *et al*. 1995). The Al_2O_3 and TiO_2 contents in our samples are generally high, 2.71–6.71 wt.% for Al_2O_3 (average at 3.72 wt.%) and 0.06–032 wt.% for TiO_2 (average at 0.13 wt.%), which are similar to those of Opx in peridotites from Ronda and Beni Bousera (Gueddari *et al*. 1996). They are distinctly higher than those secondary Opx in mantle wedges, such as Avacha in the Kamchatka arc (Russia), Iraya (Philippines), and the Colorado Plateau (USA) (Smith *et al*. 1999; Arai *et al*. 2003), and in subcratonic mantles, such as Kaapvaal (South Africa) (Kelemen *et al*. 1998; Bell *et al*. 2005). Secondary Opx in mantle wedges and subcratonic mantle forms from Ol by reacting with Si-rich melt (Kelemen *et al*. 1998; Smith *et al*. 1999; Arai *et al*. 2003; Wang *et al*. 2008b). The data suggest that the Opx in the study area are primitive and suffered very minor late modifications. As observed in Ol, grains of Opx also show slightly higher CaO contents in the rims than in the core.

Clinopyroxene

Major element abundances of Cpx are similar within a single grain and between grains in individual samples, confirming equilibrium of samples. The Cpx in xenoliths from the study areas have markedly high Al_2O_3 (3.82–7.33 wt.%) and TiO_2 (0.14–1.25 wt.%), relatively low Mg# (0.886–0.931), and wide ranges in CaO (17.23–22.65 wt.%) and Na_2O (0.43–2.15 wt.%) (Table 1).

For trace elements, studied Cpx in peridotites contains relatively low total REE, <36 ppm, and other incompatible elements (Table 2). Within individual volcanic fields, Cpx in harzburgite shows relatively higher LREE and lower HREE than that in lherzolite (Figures 3B and 3C). Three chondrite-normalized REE patterns of Cpx are recognized based on fractionation of REE (Figure 3). Type I shows a LREE-enriched pattern with negative slope from La to Eu and flat from Eu to Lu ($(La/Yb)n = 2.25–3.23$); type II has a LREE-depleted pattern with a positive slope from La to Sm and flat from Eu to Lu ($(La/Yb)n = 0.03–0.47$); type III has a roughly flat REE pattern ($(La/Yb)n = 0.73$) except several samples with slightly low contents of Ce and Pr. There is one sample, DLW6, that has high abundances of MREE and HREE and shows a 'convex' shape in REE pattern (Table 2; Figure 3). Overall, the spider diagrams of Cpx from different volcanic fields in the study area are similar in patterns (Figure 4). In individual volcanic fields, Cpx in harzburgite shows relatively higher incompatible elements than that in lherzolite (Figures 4B and 4C). The relatively high abundances of LREE and incompatible elements in harzburgite suggest that harzburgite had undergone cryptic metasomatism and that it was more susceptible to modification than that of lherzolite. The trace elements show apparent lows at Ba, Nb, Ta, Pb and Ti and the pattern is similar to that of Shanwang peridotites, which is considered to represent a new lithospheric mantle formed from upwelling asthenosphere in Mesozoic time.

Spinel

The contents of Cr in Spl reflect the degree of partial melting in the residual peridotites because Al is preferentially incorporated into a melt during partial melting. The Cr# of Spl in lherzolite and harzburgite are in the range of 0.09–0.28 and 0.22–0.36, and Mg# ($=Mg/(Mg + Fe^{2+})$) of 0.68–0.84 and 0.74–0.78, respectively, again confirming the general interpretation that harzburgite is more refractory. The contents of Fe^{3+} are low, $Y_{Fe3+} = Fe^{3+}/(Fe^{3+} + Al^{3+} + Cr^{3+}) < 0.03$, in all our samples. The values of Cr# in our samples plot in the field of abyssal peridotites (Figure 5), but far from the field of fore-arc mantle wedges in the binary Cr#–Mg# diagram. Spinel in fore-arc mantle wedges contain high Cr and Cr# >0.7 (Hattori *et al*. 2010). In the diagram of Cr# in Spl *versus* Fo in Ol in Figure 6, our samples plot within the Ol-Spl mantle array defined by Arai (1994) and near and within the field of abyssal peridotites. The data further confirm that the samples are relatively fertile residual mantle peridotites after low degrees of partial melting.

Bulk rock composition

The lherzolites in the area contain moderate Mg# (0.89–0.90), moderate concentrations of compatible elements, such as Cr (2200–3240 ppm), Co (90–108 ppm), and Ni (1500–2280 ppm), and high concentrations of moderately incompatible elements, such as Al_2O_3 (1.90–3.95 wt.%) and CaO (1.53–4.32 wt.%), which are similar to values of the primitive mantle (McDonough and Sun 1995; Table 3). They are also similar to the Shanwang periditites, which are considered to represent fertile mantle peridotites underlying the NCC (Zheng *et al*. 2005; Figure 7). In contrast, harzburgites in LG show lower Al_2O_3 (0.90–1.46 wt.%) and CaO (0.59–1.12 wt.%) and higher Mg# (~0.91), Cr (2050–3760 ppm), Ni (2400–2600 ppm), and Co (110–120 ppm) than lherzolites in the area.

Our peridotite samples show a positive correlation between Al_2O_3 and CaO with the correlation factor of 0.89. Harzburgite samples plot between xenolith samples from Heibi and Xinyang and overlap with the field of Kaapvaal low-T xenoliths. Lherzolite samples plot between Xinyang and Shangwang with one sample very close to the primitive mantle composition (Figure 7). The data suggest that our samples likely formed from a fertile mantle after melting of Cpx, the major host for CaO and Al_2O_3 in Spl-facies peridotite. Overall, our samples show compositions similar to abyssal peridotites as well as anhydrous peridotites along continental rifts and mantle plume environments, but

Table 2. LA-ICP-MS trace element analyses of clinopyroxene in the selected peridotites from the northeast margin of NCC (ppm)*.

Volcanic field	Changbaishan			Longgang									WQ	
Sample	HSW1	HSW3	HSW4	DLW3	DLW5	DLW6	DYS4	DYS5	DYS9	DYS13	LQL3	LQL4	PFS15	PFS5
Rb	0.01	0.02	0.02	0.01	0.02	0.39	0.12	0.03	bd	0.01	bd	bd	0.01	8.19
Ba	bd	0.10	0.04	0.02	0.11	11.60	0.69	0.07	0.05	0.07	0.04	bd	0.05	4.60
Th	0.01	0.54	0.06	0.02	0.19	0.12	0.05	0.33	bd	0.14	bd	0.19	0.01	1.22
U	bd	0.14	0.01	0.01	0.04	0.02	0.01	0.07	0.01	0.05	bd	0.07	0.01	0.21
Nb	bd	0.19	0.27	0.01	0.27	0.36	0.04	0.11	0.07	0.02	bd	0.15	0.03	0.20
Ta	bd	0.01	0.06	bd	0.02	0.02	0.01	0.01	0.01	0.00	bd	bd	bd	bd
La	0.06	5.71	1.46	0.08	2.21	2.07	0.55	3.01	0.35	0.59	0.14	2.87	0.34	8.10
Ce	0.61	10.94	4.55	0.76	3.65	6.70	1.44	5.19	1.49	2.29	0.98	4.49	1.55	12.19
Pr	0.22	1.21	0.82	0.30	0.44	1.16	0.29	0.58	0.37	0.52	0.33	0.50	0.32	1.12
Pb	0.04	0.39	0.15	0.03	0.07	0.26	0.36	0.08	0.03	0.07	0.08	0.19	0.08	0.45
Sr	25.33	146.74	81.44	13.74	67.49	83.50	18.48	45.34	29.50	45.93	20.05	64.15	43.19	67.13
Nd	2.09	5.14	4.96	2.39	2.43	8.24	2.48	3.49	2.82	4.35	2.73	2.02	2.18	4.45
Zr	14.18	28.92	39.70	14.16	22.32	51.73	17.16	57.54	19.33	53.25	19.79	8.32	17.92	26.99
Hf	0.67	0.90	1.04	0.76	0.61	1.38	0.84	1.77	0.68	1.60	0.95	0.25	0.55	0.67
Sm	1.03	1.76	1.85	1.32	1.02	3.09	1.32	1.44	1.25	1.79	1.57	0.74	1.11	1.24
Eu	0.51	0.69	0.73	0.56	0.46	1.04	0.52	0.62	0.67	0.83	0.58	0.31	0.46	0.67
Ti	2530	2908	3963	3033	2112	3876	2357	2573	3149	2347	2956	1482	2101	1437
Gd	2.19	2.37	2.50	2.31	1.71	3.20	2.24	1.93	2.49	2.60	1.88	0.97	1.82	1.70
Tb	0.36	0.46	0.51	0.49	0.34	0.53	0.43	0.37	0.37	0.41	0.42	0.22	0.34	0.31
Dy	2.66	2.81	3.59	3.30	2.46	3.04	3.03	2.42	3.05	2.80	3.24	1.56	2.72	2.08
Ho	0.64	0.67	0.84	0.80	0.58	0.60	0.70	0.57	0.61	0.58	0.68	0.38	0.67	0.40
Er	1.67	1.84	2.20	2.23	1.73	1.39	1.90	1.50	1.86	1.50	1.80	1.11	1.63	1.31
Tm	0.25	0.26	0.36	0.33	0.24	0.18	0.28	0.19	0.27	0.18	0.30	0.15	0.24	0.20
Y	16.36	17.60	20.80	20.48	15.45	14.35	17.66	13.95	18.11	14.15	18.01	9.74	16.13	12.35
Yb	1.64	1.77	1.99	2.31	1.76	1.21	1.76	1.43	1.91	1.25	1.82	1.05	1.60	1.42
Lu	0.25	0.27	0.31	0.33	0.23	0.15	0.27	0.17	0.22	0.18	0.30	0.15	0.26	0.20
total REE	14.17	35.90	26.69	17.51	19.28	32.59	17.19	22.92	17.74	19.88	16.79	16.53	15.25	35.39
La/Yb	0.04	3.23	0.73	0.03	1.25	1.71	0.31	2.09	0.18	0.47	0.08	2.75	0.21	5.68

Notes: bd, below determintion limits.
*The data for each sample represent average clinopyroxene composition of 3–5 grains.

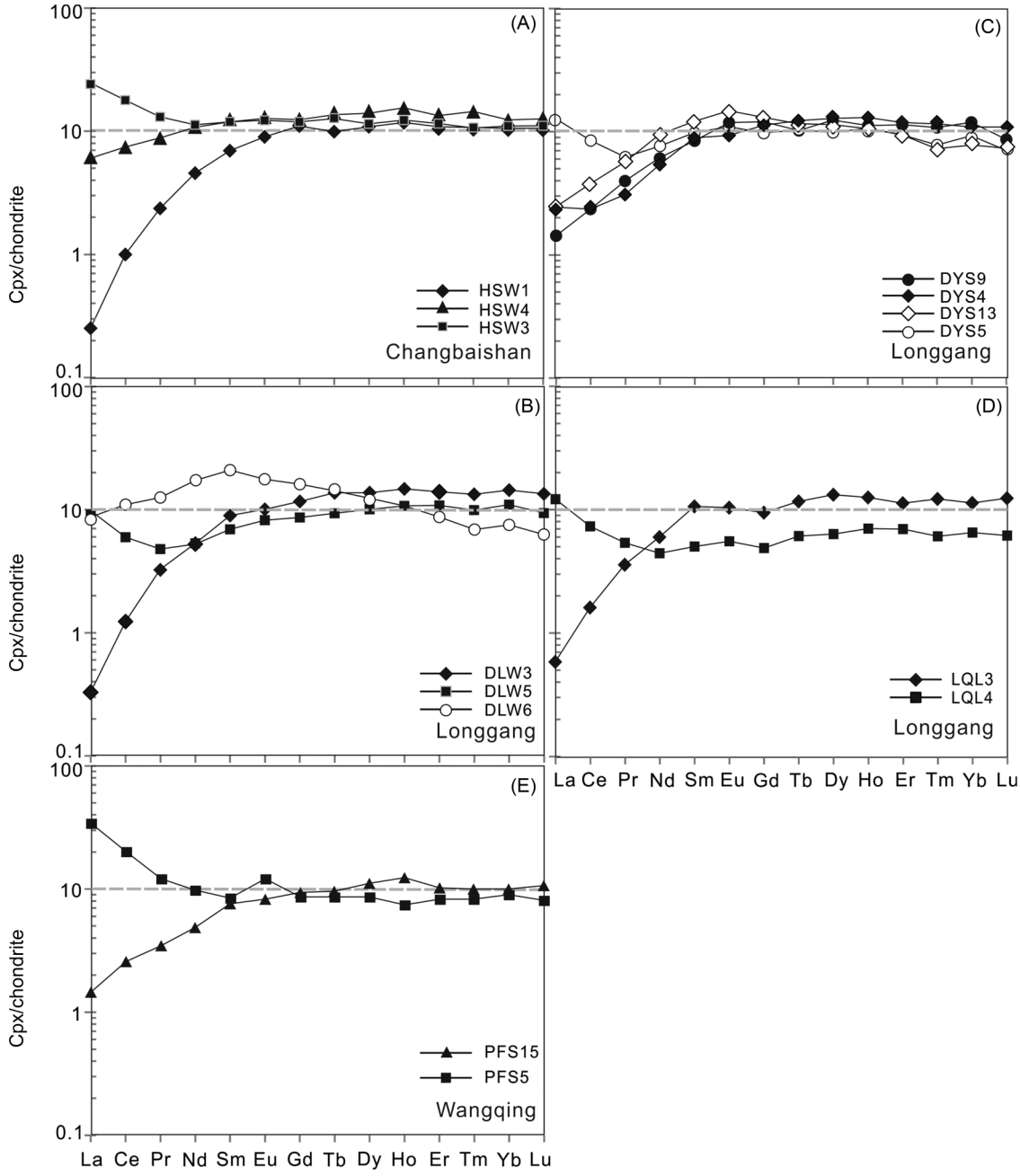

Figure 3. Representative chondrite-normalized (McDonough and Sun 1995) REE patterns of Cpx in peridotites from the north-eastern margin of NCC. (A) Hongsongwang volcano of CBS, (B) Dalongwan volcano of LG, (C) Dayizishan volcano of LG, (D) Longquanlongwan volcano of LG, and (E) Pingfengshan volcano of WQ. Open symbol represents harzburgite and solid symbol represents lherzolite.

distinctly different from peridotites from mantle wedges, suggesting that the samples have undergone a low degree of partial melting and later modifications are minor if any occurred.

Estimates of Temperatures and fO_2

Grains of Ol, Opx, and Spl show similar composition in individual samples and no differences (<5%) were observed for major element abundance between core and rim areas in individual grains. Furthermore, the Mg# of Opx and Fo of Ol show a positive correlation among our samples, suggesting that the equilibrium has been reached in the studied mantle rocks. This is the basis for estimating equilibrium pressures, temperatures, and fO_2 of these xenoliths.

Temperatures for our peridotite xenoliths were determined using two-pyroxene thermometers of Wells (1977)

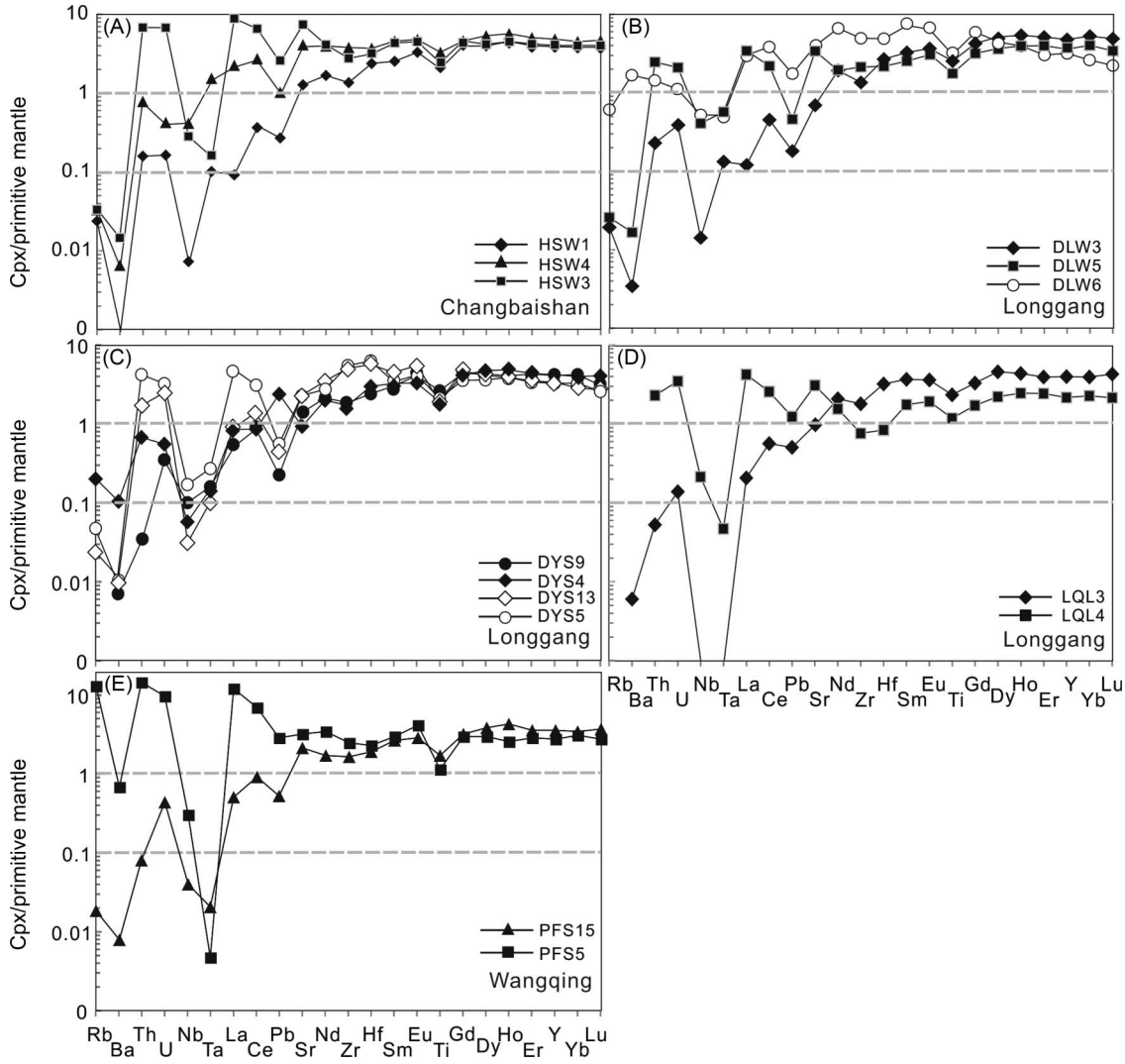

Figure 4. Representative primitive mantle-normalized (McDonough and Sun 1995) trace element patterns of Cpx in peridotites from the northeastern margin of NCC. Symbols are the same as Figure 3.

and Brey and Köhler (1990), Ca-in-Opx thermometry of Brey and Köhler (1990), and Ol-spinel Fe-Mg exchange thermometry of Ballhaus *et al*. (1991). The thermometry of Ballhaus *et al*. (1991) gives systematically lower temperatures than other three thermometers, most likely due to its low closure temperature for Fe-Mg ion exchange between Spl and Ol (e.g. DeHoog *et al*. 2004) (Table 4). Overall, no significant differences (<50°C) were observed among the other three thermometers except one sample, HSW2, which yielded much higher temperature (1170°C) using the Ca-in-Opx thermometer than 917°C and 937°C using two different two-pyroxene thermometers. The two-pyroxene thermometry of Brey and Köhler (1990) was used to calculate temperatures for fO_2 calculation in this study because it was commonly used for mantle peridotites by previous workers. The results are listed in Table 4.

The oxidation state is estimated based on the oxygen barometry of Nell and Wood (1991). No apparent fO_2 differences were observed between lherzolites and harzburgites in the study area (Table 5). The fO_2 values for all our samples range from FMQ –2.64 to +0.39 with an average at FMQ –0.59 ($n = 53$), which are comparable to abyssal peridotites (Figure 8) and peridotite massifs from Ronda and Beni Bousera (Wood *et al*. 1990). These massifs are considered to represent tectonically protruded asthenospheric mantle peridotites. The obtained values are also similar to fO_2 values of SCLM affected by upwelling asthenosphere in an extension regime (Figure 8), such as Baikal rift Zone and Dariganga in Central Asia (Ionov and Wood 1992), Kilbourne Hole and San Carlos in North America (Wood *et al*. 1990), and Pali Aike in South America (Wang *et al*. 2008a).The values of fO_2 are much lower than those for sub-arc mantle peridotites (Figure 8), such as Ichinomegata (Wood *et al*. 1990) and southwest Japan (Arai and Ishimaru 2008), Sikhote-Alin Ridge and Avacha in Russia (Ionov and Wood 1992; Arai *et al*. 2003),

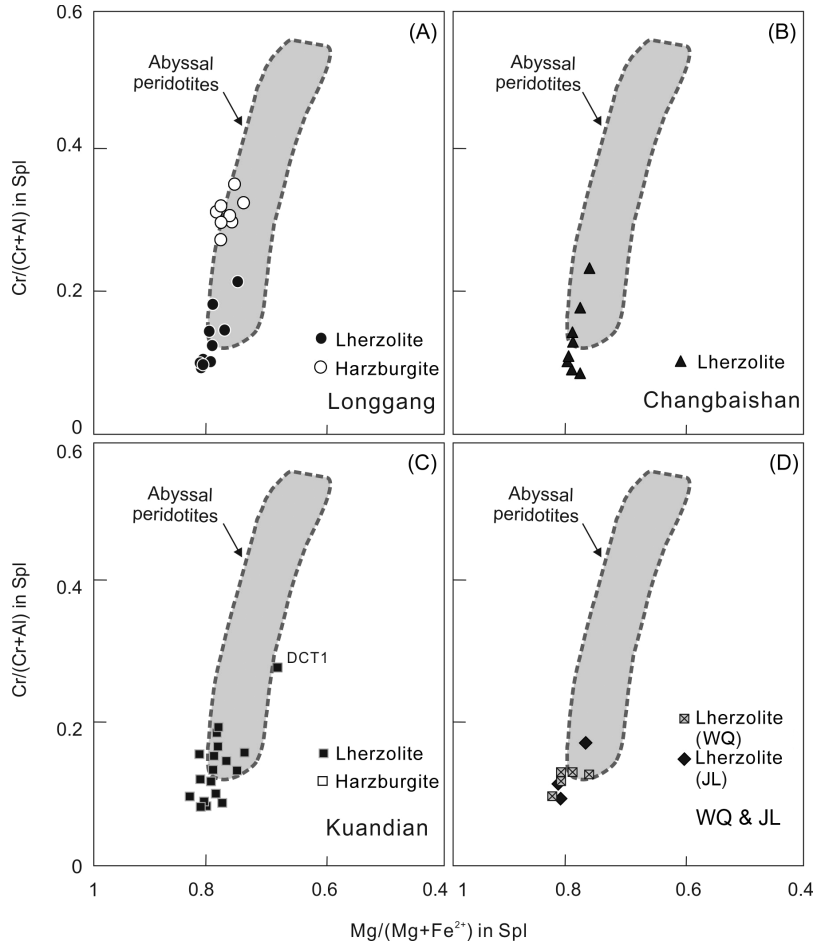

Figure 5. Plot of Cr# *versus* Mg/(Mg + Fe^{2+}) for spinel in peridotites from the NE margin of NCC and southern margin of XMOB (A = Longgang; B = Changbaishan; C = Kuandian; D = WQ and JL), compared with the data for abyssal peridotites (Dick and Bullen 1984). Data of Changbaishan are from Wang *et al*. (2012b). Each point is a representative analysis of a Spl grain in each thin section. Open symbol represents harzburgite and solid symbol represents lherzolite.

Simcoe in the USA (Parkinson and Arculus 1999), and Laiwu in China (Wang *et al.* 2012a).

Discussion

Partial melting

The coexistence of lherzolites and harzburgites in the study area and variable Cr# in Spl in xenoliths suggests variable degrees of partial melting in the mantle below the study area. In the bulk rock plot of Al_2O_3–CaO (Figure 7), the studied samples show a positive correlation, and one sample (HSW2) has a composition very similar to the primitive mantle composition (McDonough and Sun 1995), suggesting that they are likely formed from a relatively fertile mantle after melting of Cpx, which is the major host for CaO and Al_2O_3 in Spl-facies peridotite.

The values Cr# in Spl and coexisting Cpx are a sensitive indicator of the degree of partial melting. The samples show compositional relations of Fo in Ol and Cr# in Spl (Figure 6) and between Cr# in Cpx and Cr# in Spl (not shown). These data also support that the samples represent mantle peridotites after small, but variable degrees of partial melting. The low values of Cr# of Spl < 0.35) and that of Cpx, <0.22, in most samples indicate that the peridotites in the study area are residues after a small volume of melt extraction.

Clinopyroxene is the major host for incompatible trace elements in Spl-facies anhydrous peridotites. Moderately incompatible elements, such as Y and Yb, in Cpx can be used to evaluate the degree of partial melting since these elements are less susceptible to mantle metasomatism (Johnson *et al*. 1990; Norman 1998). We modelled Y and Yb contents in Cpx with $K_d = 0.42$ for Yb and $K_d = 0.40$ for Y between Cpx and melt (Norman 1998) and the primitive mantle compositions (McDonough and Sun 1995). The calculations of both batch and fractional melting show that the lherzolites in LG, CBS, and WQ formed after less than 4% partial melting (Figure 9) and that the

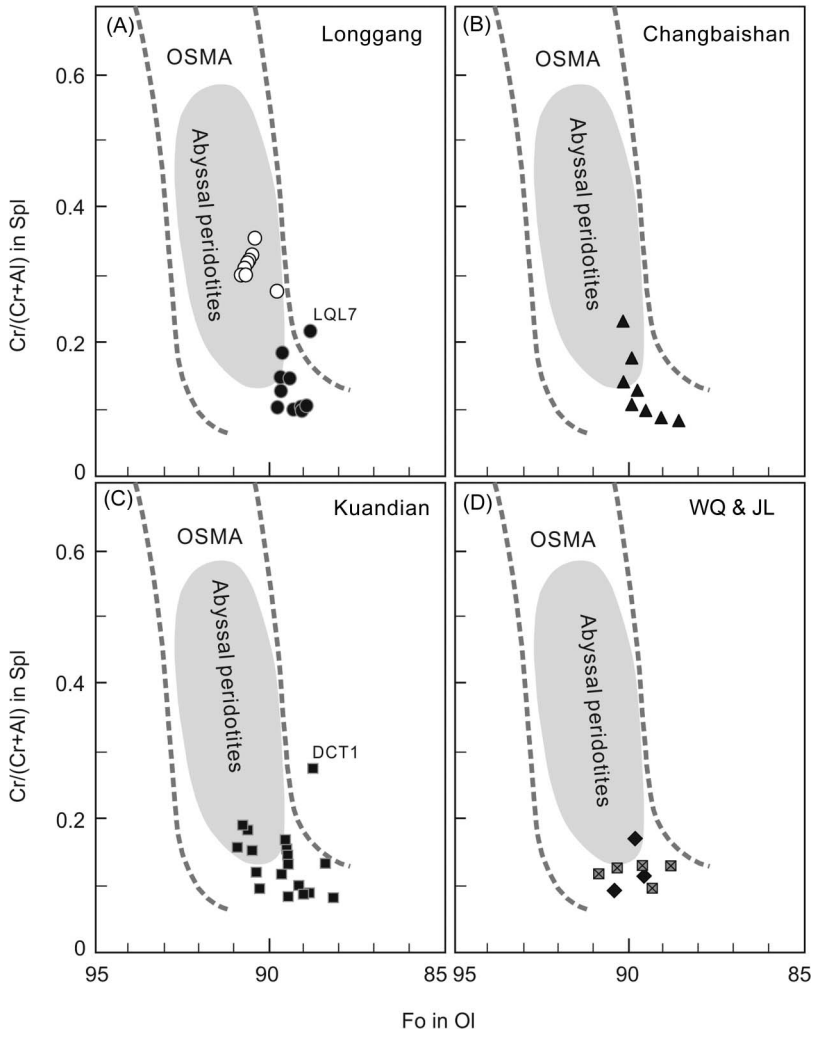

Figure 6. Fo component of olivine and Cr# of spinel in peridotite xenoliths from the northeast margin of NCC and southern margin of XMOB (A = Longgang; B = Changbaishan; C = Kuandian; D = WQ and JL). Symbols are the same as Figure 5. Data of Changbaishan are from Wang *et al*. (2012b). Note that only two samples (LQL7 and DCT1) plot outside the olivine-spinel mantle array (OSMA) defined by Arai (1994), while all others plot inside OSMA, suggesting that most xenoliths from the study area are primary mantle peridotites. It also shows the field of abyssal peridotite as a shaded area (Arai 1994).

harzburgites in LG are residues of slightly high degrees of partial melting (4–5% for fractional melting or 5–6% for batch melting). The results are consistent with the general interpretation that harzburgite has undergone higher degrees of partial melting than lherzolite.

Metasomatism

Although no metasomatic minerals were found in our mantle xenoliths, Shi *et al*. (1999) reported the presence of phlogopite and amphibole in mantle xenoliths from volcanic rocks including those at Jinlongdingzi and Hongqilinchang volcanoes in the LG volcanic field. Mineral chemistry of peridotites from this study provides the evidence for cryptic mantle metasomatism. For example, sample LQL7 (harzburgite) from LG and sample DCT1 (lherzolite) from the KD volcanic field plot outside the Ol-spinel mantle array of Arai (1994) (Figure 6), suggesting that Fo components of Ol were lowered by a metasomatic agent with low Mg#.

Trace elements of Cpx provide the further evidence supporting the metasomatism. The Cpx from LG, CBS, and WQ have very low $(La/Yb)_n$ (<5) and high Ti/Eu (2800–5300), close to the Cpx field of Cenozoic Shanwang xenoliths in the NCC, which are considered to represent asthenosphere-derived, newly formed SCLM (Figure 10; Zheng *et al*. 2005). Our data plot in a narrow field in the diagram of $(La/Yb)_n$ *versus* Ti/Eu. Among them, HSW4 and DYS9 are very close to the primitive mantle values in terms of bulk rock and mineral compositions and do not show any evidence of metasomatism. They are different from those of Palaeozoic kimberlite-hosted

Table 3. Major and trace element abundances of selected mantle xenoliths from the northeast margin of NCC and southern margin of XMOB.

Volcanic field	Longgang													
Sample lithology	DLW1 Harz	DLW6 Harz	DLW3 Lher	DLW5 Lher	DYS1 Harz	DYS5 Harz	DYS7 Harz	DYS12 Harz	DYS13 Harz	DYS14 Harz	DYS9 Lher	LQL3 Lher	LQL4 Lher	LQL8 Lher
Major elements (wt.%)														
SiO_2	43.80	42.80	44.44	44.30	43.15	41.36	41.24	42.72	43.40	45.00	44.23	43.75	43.47	44.53
TiO_2	0.10	0.11	0.11	0.09	0.06	0.05	0.05	0.06	0.05	0.11	0.11	0.09	0.05	0.11
Al_2O_3	0.90	0.90	3.58	2.40	1.36	1.16	1.10	1.46	1.40	1.40	3.02	2.29	1.93	3.21
Fe_2O_3(T)	8.90	8.90	8.95	9.20	8.90	9.04	9.13	8.94	8.90	8.50	9.07	9.24	9.46	9.45
MnO	0.12	0.12	0.13	0.13	0.13	0.13	0.13	0.13	0.12	0.12	0.14	0.13	0.14	0.14
MgO	45.58	46.16	38.60	42.01	44.72	44.88	45.53	44.92	45.43	44.21	40.01	41.28	42.24	39.11
CaO	0.97	0.59	3.19	2.13	0.77	0.66	0.60	1.12	1.06	0.99	2.72	2.44	1.79	2.98
K_2O	0.02	0.02	<0.01	0.01	0.01	<0.01	0.02	0.01	0.02	0.01	0.00	<0.01	<0.01	<0.01
P_2O_5	<0.01	0.01	0.01	0.01	0.01	0.01	0.01	0.01	<0.01	<0.01	0.01	0.01	0.01	0.01
Total	100.39	99.60	99.01	100.27	99.34	97.51	98.14	99.74	100.38	100.34	99.60	99.57	99.25	99.81
Mg#	0.91	0.91	0.90	0.90	0.91	0.91	0.91	0.91	0.91	0.91	0.90	0.90	0.90	0.89
Trace elements in ppm														
Cr	2053	2189	2633	2600	3221	3069	3018	3755	nd	nd	2433	2530	2423	2243
Co	nd	nd	95	nd	111	109	119	111	nd	nd	98	103	105	103
Ni	nd	nd	1907	nd	2396	2477	2605	2440	nd	nd	2088	2165	2245	1945

(*Continued*)

Table 3. (Continued).

Volcanic field	WQ					Kuandian			
Sample lithology	PFS5 Lher	PFS9 Lher	PFS13 Lher	PFS15 Lher	PFS16 Lher	HYS4 Lher	QYS8 Lher	QYS15 Lher	DCT9 Lher
Major elements (wt.%)									
SiO_2	43.77	42.44	43.31	43.58	45.13	43.71	44.59	42.62	43.94
TiO_2	0.10	0.05	0.06	0.08	0.10	0.14	0.32	0.25	0.11
Al_2O_3	2.69	1.99	2.30	2.81	3.27	3.36	3.25	3.16	2.47
Fe_2O_3(T)	9.30	9.06	9.34	8.82	8.54	9.07	8.36	9.56	9.36
MnO	0.14	0.14	0.14	0.13	0.13	0.13	0.13	0.14	0.13
MgO	40.80	40.62	41.51	39.38	38.52	37.77	37.71	38.46	40.84
CaO	2.30	1.64	2.01	2.89	3.35	3.27	4.32	2.33	2.20
K_2O	0.14	0.11	0.10	0.01	<0.01	0.01	0.02	0.14	0.02
P_2O_5	0.02	0.01	0.03	0.01	0.01	0.01	0.01	0.06	0.01
Total	99.69	96.42	99.16	98.07	99.35	97.88	99.16	97.41	99.47
Mg#	0.90	0.90	0.90	0.90	0.90	0.89	0.90	0.89	0.90
Trace elements in ppm									
Cr	2263	2810	2595	2651	2402	2381	3245	2485	2277
Co	108	108	107	103	99	98	90	103	106
Ni	2199	2212	2282	2115	2008	2005	1843	1505	2265

Note: nd, not determined.

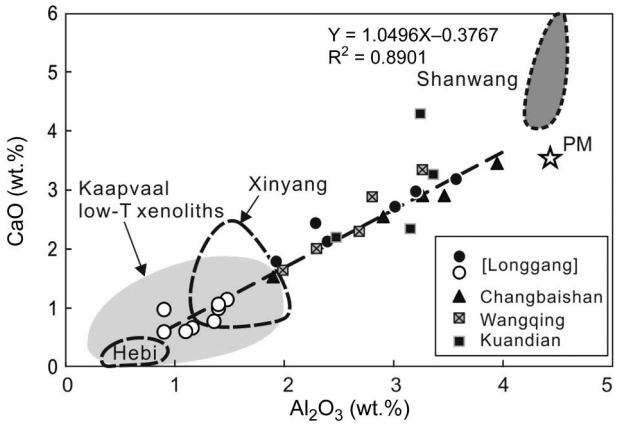

Figure 7. Plot of CaO *versus* Al_2O_3 for spinel lherzolites from the northeast margin of NCC and southern margin of XMOB. Symbols are the same as Figure 5. The large open star represents primitive mantle (PM) from McDonough and Sun (1995). Data source for peridotites includes Xinyang, Hebi, Shanwang and Kaapvaal low-T xenoliths compiled by Zheng *et al*. (2005). Data of Changbaishan are from Wang *et al*. (2012a). Note that our samples plot in between Hebi and PM and show linear positive correlation.

mantle xenoliths at Mengyin and Donghai, which are metasomatized by carbonatitic melt and show variably high $(La/Yb)_n$ (>20) and low Ti/Eu (<1500) in Cpx (Figure 10). High contents of LREE combined with low high-field-strength elements are typically found in mantle Cpx affected by carbonatitic metasomatism (Yaxley *et al*. 1998). Therefore, our data suggest that the mantle xenoliths from the study area are either free of carbonatitic metasomatism or slightly modified by silicate melt.

Reaction with metasomatic agents produces a variety of REE patterns, notably variable enrichment in LREE because they are mobile and high in concentrations in melt and also in fluids (Bodinier *et al*. 2004). On the other hand, residual mantle peridotites contain low LREE and are susceptible to acquiring LREE from metasomatic agents. This explains the observed variable REE and incompatible elemental patterns of Cpx with similar major oxide contents in the study areas (Figures 3 and 4).

Evolution of SCLM below the northeastern margin of the NCC

It has been well established that the SCLM below the NCC was very thick, over 200 km, until the beginning of Mesozoic time (e.g. Kusky *et al*. 2007). It is a major question how and why this thick SCLM transformed into thin lithosphere similar to oceanic lithosphere in the eastern NCC. A number of possible models have been proposed, including: (1) model I, thermal–chemical erosion of the lithosphere by asthenosphere, probably a mantle plume, as a result of enhanced mantle convection caused by Pacific oceanic subduction underneath the eastern Asian continent (Xu 2001); (2) model II, delamination of thickened lithosphere due to the collision of North China Craton and the Yangtze Craton (Gao *et al*. 2002, 2004; Yang *et al*. 2003; Deng *et al*. 2007); and (3) model III, delamination of thickened lithosphere coupled with upwelling asthenosphere triggered by subduction of the Pacific oceanic plate (Wu *et al*. 2003, 2011).

Model I considers that a hot uprising mantle plume heated and metasomatized the lower part of the lithosphere and eventually change it into lithosphere of asthenospheric composition during late Mesozoic time. However, our peridotite samples show a linear positive correlation between Al_2O_3 and CaO, suggesting that the compositional variation is due to different degrees of partial melting instead of extensive metasomatism. The data indicate that the metasomatism, if any, did not significantly modify the major element abundance in the mantle peridotites. This is supported by the compositions of Spl and Ol in all LG, CBS, KD, WQ, and JL peridotites, which plot within the mantle array (Figure 6). Metasomatism lowers Fo of Ol and Cr# of Spl. A slightly modified model, 'hydration weakening–thermal convection transformation', was proposed by Niu (2005), where the present-day fertile SCLM formed by extensive hydration of ancient refractory mantle with aqueous fluid/melt released from the subducted Pacific oceanic crust. We discount this proposal because aqueous fluid or subduction-related H_2O-rich melt would form hydrous minerals, such as amphiboles and clinochlore, but these were not observed in the area. In addition, the acquired fO_2 data in this study do not support this model because the metasomatism in mantle wedges generally raise fO_2 values. Instead, mantle xenoliths in the LG, KD, CBS, WQ, and JL volcanoes yielded fO_2 values similar to that of asthenospheric mantle.

Model II emphasizes that the collision between the Yangtze plate and the NCC has thickened the already-thick SCLM, and the mechanical instability resulted in the removal of the deep part of lithosphere. The study area is located in the northeastern margin of NCC and southern margin of the late Palaeozoic XMOB, but far (over 1500 km) from the Dabie-Sulu UHP Belt (Figure 1). Therefore, the newly formed Mesozoic mantle beneath the study area was unlikely related to the collision of Yangtze with NCC. People may argue that collision of the late Palaeozoic XMOB with the northern margin of NCC led to the removal of the lower part of SCLM in the study area. We discount this possibility because the final closure of the Palaeo-Asian ocean and amalgamation of the late Palaeozoic XMOB with NCC occurred at the end of the late Palaeozoic (ca. 250 Ma; Wu *et al*. 2011), earlier than the formation age (early to middle Mesozoic) of the mantle in the area.

In the last decade, researchers have recognized that the subduction of the Pacific oceanic plate had triggered the

Table 4. Estimated equilibration temperatures for peridotites from the Cenozoic volcanic fields in the northeast margin of NCC and southern margin of XMOB.

Volcanic field	Volcanos	Sample	TBK(90)-2px (°C)[a]	TBK(90) Ca-in-Opx (°C)[b]	TWells(77) (°C)[c]	TB(91) (°C)[d]
Longgang	Dalongwan	DLW1	1144	1088	1118	965
		DLW3	1027	927	991	937
		DLW5	1075	1021	1063	937
		DLW6	1012	905	991	956
		DLW8	842	880	886	961
	Dayizishan	DYS1	1030	969	1015	938
		DYS4	950	977	977	977
		DYS5	1023	990	1032	1035
		DYS7	1026	1002	1027	1001
		DYS9	894	912	920	812
		DYS12	963	925	968	855
		DYS13	1070	1001	1068	900
		DYS14	910	917	921	873
	Longquanlongwan	LQL1	1135	1036	1105	1000
		LQL3	858	891	912	769
		LQL4	1077	1024	1050	950
		LQL6	1031	986	1038	828
		LQL7	987	992	993	866
		LQL8	1088	1068	1058	999
	Average		1007	974	1007	924
Kuandian	Dachuangtou	DCT1	940	960	939	757
		DCT2	925	856	948	813
		DCT3	898	868	906	798
		DCT5	1133	1088	1123	991
		DCT8	976	960	980	874
		DCT9	1139	1100	1131	1054
	Huangyishan	HYS1	755	880	820	822
		HYS2	811	856	850	821
		HYS4	741	868	819	730
		HYS7	768	843	830	932
		HYS13	1213	1154	1232	727
		HYS14	895	902	926	806
		HYS24	767	891	834	*nd*
		HYS26	1026	960	1070	981
	Qingyishan	QYS8	988	960	997	646
		QYS10	956	891	906	777
		QYS14	1010	960	1010	770
		QYS15	1104	1018	1073	868
		QYS18	1044	1018	1048	934
	Average		953	948	972	844
WQ	Pingfengshan	PFS5	880	912	933	689
		PFS15	896	856	904	814
		PFS16	876	880	907	1005
	Average		884	883	914	836
JL	Qiantuanshan	QTS8	886	912	915	nd
		QTS5	1004	1002	1018	958
	Houtuanshan	HTS6	891	922	942	780
		HTS9	915	986	945	836
	Average		924	956	955	858

Notes: nd, not determined.
[a]Brey and Köhler (1990) two-pyroxene thermometer.
[b]Brey and Köhler (1990) Ca-in-Opx thermometer.
[c]Wells (1977) two-pyroxene thermometer.
[d]Ballhaus *et al*. (1991) Ol-Spl Mg–Fe exchange thermometer.

destruction of NCC. For example, Xu *et al*. (2011) documented the contribution of subduction-related components in Cenozoic basalts in the eastern NCC and suggested that the subduction of Pacific oceanic plates had played a key role in the destruction of NCC. Similarly, Windley *et al*. (2011) have noticed that the eastern NCC is bounded by the south-dipping Solonker suture (Permo-Triassic) and Mongol-Okhotsk suture (Jurassic) to the north, by

Table 5. Estimates of oxygen fugacity values for the mantle xenoliths from the NE margin of NCC and southern margin of XMOB.

Volcanic field	Longgang																		
Sample lithology[a]	DLW1 harz	DLW3 Lher	DLW5 lher	DLW6 harz	DLW8 lher	DYS1 harz	DYS4 lher	DYS5 harz	DYS7 harz	DYS9 lher	DYS12 harz	DYS13 harz	DYS14 harz	LQL1 harz	LQL3 lher	LQL4 lher	LQL6 lher	LQL7 lher	LQL8 lher
Olivine																			
X_{Fe}	0.096	0.107	0.106	0.093	0.108	0.093	0.109	0.093	0.094	0.102	0.094	0.093	0.092	0.102	0.103	0.103	0.103	0.112	0.110
X_{Mg}	0.904	0.893	0.894	0.907	0.892	0.907	0.891	0.907	0.906	0.898	0.906	0.907	0.908	0.898	0.897	0.897	0.897	0.888	0.890
Orthopyroxene																			
$M1_{(Fe)}$[b]	0.081	0.091	0.089	0.080	0.094	0.081	0.094	0.081	0.079	0.090	0.082	0.078	0.080	0.086	0.089	0.091	0.086	0.096	0.097
$M2_{(Fe)}$[b]	0.081	0.096	0.094	0.084	0.099	0.083	0.101	0.084	0.083	0.093	0.086	0.081	0.082	0.087	0.094	0.090	0.089	0.096	0.098
Spinel																			
Cr#	0.355	0.100	0.146	0.301	0.101	0.310	0.098	0.317	0.322	0.103	0.329	0.310	0.302	0.276	0.148	0.184	0.127	0.217	0.108
$Fe^{3+}/\sum Fe$[c]	0.216	0.230	0.245	0.233	0.216	0.221	0.289	0.272	0.260	0.171	0.182	0.185	0.203	0.259	0.125	0.259	0.126	0.234	0.302
$Mg/(Mg+Fe^{2+})$	0.759	0.815	0.802	0.782	0.818	0.774	0.813	0.791	0.781	0.799	0.743	0.767	0.763	0.782	0.775	0.796	0.797	0.753	0.813
$\log a_{Fe3O4}^{Spl}$	−2.370	−2.099	−2.104	−2.206	−1.882	−2.256	−1.740	−2.122	−2.129	−2.118	−2.267	−2.443	−2.139	−2.190	−2.322	−2.078	−2.531	−1.932	−1.890
P (Gpa)[d]	1.500	1.500	1.500	1.500	1.500	1.500	1.500	1.500	1.500	1.500	1.500	1.500	1.500	1.500	1.500	1.500	1.500	1.500	1.500
TBK(90)-2px (°C)[e]	1144	1027	1075	1012	842	1030	950	1023	1026	894	963	1070	910	1135	858	1077	950	987	1088
T(°C)[f]	965	937	937	956	961	938	977	1035	1001	812	855	900	873	1000	769	950	828	866	999
$\triangle \log (fO_2)$ FMQ[g]	−0.463	−0.466	−0.304	−0.393	−0.697	−0.427	0.004	−0.211	−0.214	−0.675	−0.571	−0.694	−0.420	−0.300	−1.149	−0.201	−1.381	−0.154	0.029
$\triangle \log (fO_2)$ FMQ[h]	−0.447	−0.224	−0.176	−0.141	−0.082	−0.207	0.384	0.051	−0.038	−0.318	−0.342	−0.585	−0.125	−0.243	−0.835	−0.048	−1.211	−0.095	0.236

(*Continued*)

Table 5. (Continued).

Volcanic field	Kuandian																	
Sample lithology[a]	DCT1 lher	DCT2 lher	DCT3 lher	DCT5 lher	DCT8 lher	DCT9 lher	HYS1 lher	HYS2 lher	HYS4 lher	HYS7 lher	HYS13 lher	HYS14 lher	HYS26 lher	QYS8 lher	QYS10 lher	QYS14 lher	QYS15 lher	QYS18 lher
Olivine																		
X_{Fe}	0.112	0.093	0.095	0.097	0.096	0.105	0.105	0.103	0.109	0.111	0.105	0.092	0.118	0.090	0.108	0.105	0.105	0.116
X_{Mg}	0.888	0.907	0.905	0.903	0.904	0.895	0.895	0.897	0.891	0.889	0.895	0.908	0.882	0.910	0.892	0.895	0.895	0.884
Orthopyroxene																		
$M1_{(Fe)}$[b]	0.104	0.084	0.077	0.089	0.083	0.087	0.090	0.088	0.095	0.096	0.085	0.086	0.090	0.085	0.083	0.089	0.089	0.095
$M2_{(Fe)}$[b]	0.104	0.088	0.078	0.091	0.084	0.088	0.092	0.089	0.096	0.096	0.087	0.089	0.094	0.088	0.087	0.097	0.097	0.103
Spinel																		
Cr#	0.282	0.189	0.156	0.098	0.123	0.159	0.086	0.120	0.090	0.092	0.135	0.195	0.084	0.161	0.103	0.149	0.170	0.137
$Fe^{3+}/\sum Fe$[c]	0.232	0.128	0.113	0.250	0.125	0.252	0.111	0.107	0.088	0.226	0.201	0.148	0.160	0.137	0.063	0.066	0.151	0.177
$Mg/(Mg+Fe^{2+})$	0.684	0.788	0.793	0.835	0.817	0.818	0.806	0.798	0.779	0.810	0.754	0.785	0.815	0.741	0.790	0.772	0.787	0.795
$\log a_{Fe3O4}^{Spl}$	−1.741	−2.543	−2.590	−2.260	−2.683	−2.262	−2.249	−2.436	−2.312	−1.628	−2.208	−2.360	−2.429	−2.323	−3.096	−3.140	−2.585	−2.336
P (Gpa)[d]	1.500	1.500	1.500	1.500	1.500	1.500	1.500	1.500	1.500	1.500	1.500	1.500	1.500	1.500	1.500	1.500	1.500	1.500
TBK(90)-2px (°C)[e]	940	925	898	1133	976	1139	755	811	741	768	1213	895	1026	988	956	1010	1104	1044
T(°C)[f]	757	813	798	991	874	1054	822	821	730	932	727	806	981	646	777	770	868	934
$\triangle \log (fO_2)$ FMQ[g]	0.285	−1.255	−1.466	−0.400	−1.533	−0.558	−1.608	−1.676	−1.692	−0.504	0.091	−0.934	−1.418	−0.252	−2.524	−2.345	−1.106	−1.051
$\triangle \log (fO_2)$ FMQ[h]	0.393	−0.851	−1.330	−0.038	−1.250	−0.484	−1.016	−1.254	−1.244	0.126	−0.354	−0.418	−1.418	−0.133	−2.640	−2.268	−1.019	−0.923

(*Continued*)

Table 5. (Continued).

Volcanic field	WQ					JL		
Sample lithology[a]	PFS5 lher	PFS10 lher	PFS13 lher	PFS15 lher	PFS16 lher	QTS5 lher	HTS6 lher	HTS9 lher
Olivine								
X_{Fe}	0.096	0.112	0.104	0.091	0.106	0.104	0.102	0.096
X_{Mg}	0.904	0.888	0.896	0.909	0.894	0.896	0.898	0.904
Orthopyroxene								
$M1_{(Fe)}$[b]	0.085	0.097	0.089	0.084	0.084	0.087	0.084	0.089
$M2_{(Fe)}$[b]	0.087	0.102	0.093	0.087	0.088	0.089	0.086	0.091
Spinel								
Cr#	0.129	0.132	0.132	0.119	0.098	0.116	0.174	0.094
$Fe^{3+}/\sum Fe$[c]	0.153	0.167	0.220	0.115	0.175	0.231	0.121	0.186
$Mg/(Mg+Fe^{2+})$	0.766	0.795	0.815	0.814	0.829	0.816	0.772	0.815
$\log a_{Fe3O4}{}^{Spl}$	−2.087	−2.159	−2.097	−2.607	−2.214	−2.102	−2.448	−2.134
P (Gpa)[d]	1.500	1.500	1.500	1.500	1.500	1.500	1.500	1.500
TBK(90)-2px (°C)[e]	880	890	956	896	876	1004	891	915
T (°C)[f]	689	890	956	814	1005	958	780	836
$\triangle \log (fO_2)$ FMQ[g]	−0.352	−1.043	−0.636	−1.478	−1.294	−0.500	−1.280	−0.560
$\triangle \log (fO_2)$ FMQ[h]	−0.170	−0.629	−0.259	−0.928	−0.909	−0.304	−1.155	−0.042

Notes: [a]harz, harzburgite; lher, lherzolite.
[b]M1 (Fe) and M2 (Fe), Fractions of Fe at M1 and M2 sites, calculated following the method in Wood *et al.* (1990).
[c]$Fe3^{+}$ contents of spinel calculated from its stoichiometric composition.
[d]Pressure is assumed as 1.5 Gpa in fO_2 calculation.
[e]Temperature for Opx-Cpx bearing samples is calculated based on two-pyroxene thermometer of Brey and Köhler (1990).
[f]Calculated based on Ol-Spl Fe-Mg exchange thermometer of Ballhaus *et al.* (1991).
[g]fO_2 estimates following the method of Ballhaus *et al.* (1991).
[h]fO_2 estimates following the method of Nell and Wood (1991) using the calibrated contents of Fe^{3+}.

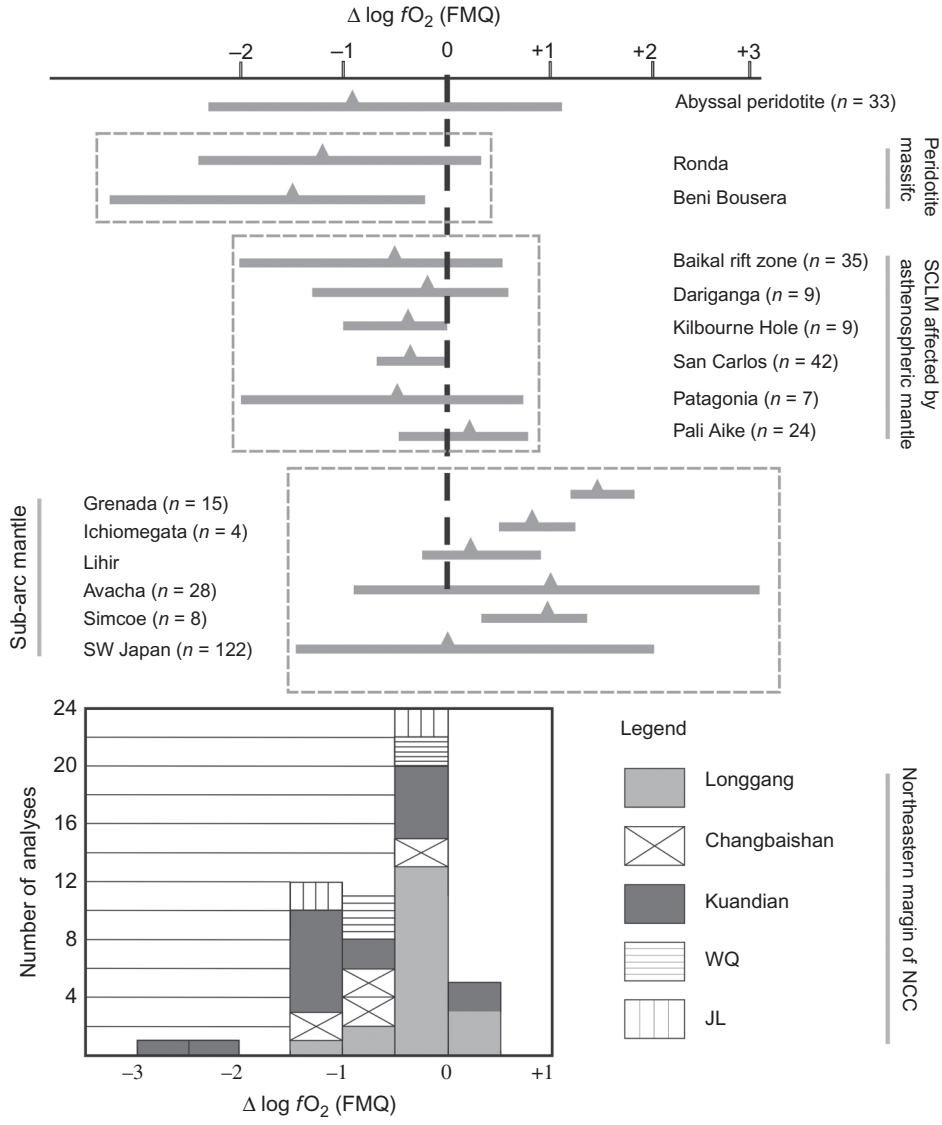

Figure 8. Oxygen fugacities (range and median value) calculated for peridotites from the northeast margin of NCC and southern margin of XMOB and compared with other tectonic settings. Measurements from the same setting are grouped within the grey dashed rectangles. The data source includes abyssal peridotites (Bryndzia and Wood 1990), peridotite massifs (Woodland *et al*. 1992; Woodland *et al*. 2006), SCLM affected by asthenosphere (Ionov and Wood 1992; Arai and Ishimaru 2008; Wang *et al*. 2008a), and peridotites from subduction settings (Wood and Virgo 1989; Brandon and Draper 1996; McInnes *et al*. 2001; Parkinson *et al*. 2003; Arai and Ishimaru 2008). Data of Changbaishan are from Wang *et al*. (2012b). Note that the fO_2 values of the NE margin of NCC and southern margin of XMOB are overlapping with those of abyssal peridotites, continental xenoliths representing SCLM affected by upwelling asthenosphere, and of peridotite massifs representing tectonically protruded asthenospheric mantle.

the north-dipping Dabieshan and Songma sutures (Permo-Triassic) to the south, and subducted by the Pacific oceanic plate to the east (start from 200 Ma). Since these sutures represent the collision of other continents after the closure of intervening oceans, large amounts of water were transported down to the mantle by subduction of oceanic plates from all directions. Windley *et al*. (2011) suggested that the huge amounts of water have played the most important role for the thinning/delamination of SCLM beneath the eastern NCC. They emphasized that delamination of the root of thickened lithosphere occurred at both northern and southern margins of the NCC, and that part of the root was chemically transformed and replaced by upwelling fertile asthenospheric material, which fed the extrusion in the Cenozoic of extensive alkali flood basalts. However, this model cannot explain why the Cenozoic basalts and enclosed fertile mantle xenoliths are distributed not only in eastern NCC but also in XMOB of eastern China.

Model III combines the above two models and suggests that the west-subducting Pacific ocean plate since

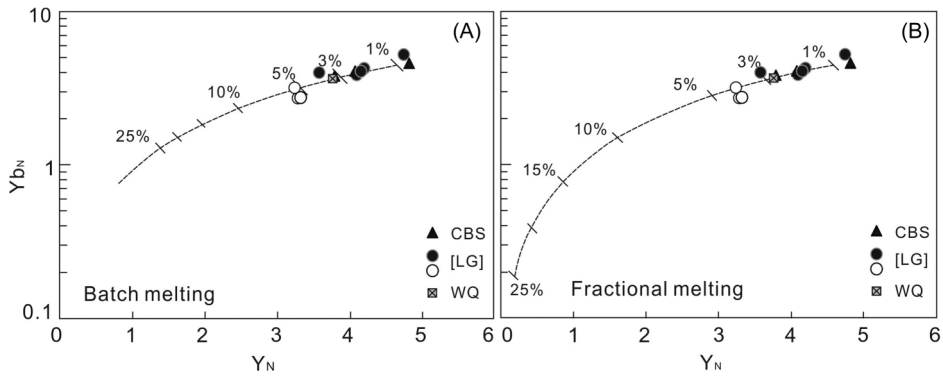

Figure 9. Diagram of Yb_N *versus* Y_N for partial melting modelling with an assumption of a primitive mantle source. Symbols are the same as Figure 5. The subscript 'N' denotes the primitive mantle-normalized element abundances (McDonough and Sun 1995). Partition coefficients (D_{Cpx}), Y (0.42), Yb (0.40), and equations of Norman (1998) are used for modelling.

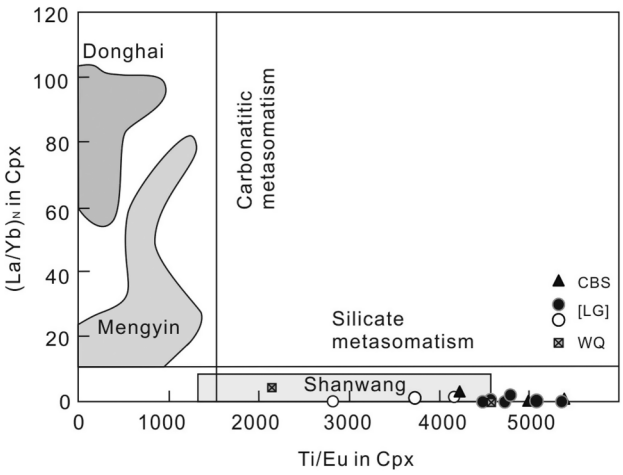

Figure 10. Ti/Eu *versus* $(La/Yb)_N$ for Cpx in the peridotites from the northeast margin of NCC. Symbols are the same as Figure 5. The subscript 'N' denotes the chondrite-normalized element abundances (Sun and McDonough 1995). Data for Donghai, Mengyin and Shanwang peridotites are from Zheng *et al*. (2006). Signatures of silicate and carbonatitic metasomatism are modified after Coltorti *et al*. (1999).

early the Mesozoic (ca. 200 Ma) was the main cause of this lithospheric removal, which was coupled with the upwelling of asthenospheric material. This model is mainly based on the observation that Phanerozoic SCLM resides not only beneath the eastern NCC but also beneath the Palaeozoic XMOB, and that the SCLM beneath southeastern and central eastern China also shows the evidence for the modification of SCLM in Mesozoic time (Zhi *et al*. 2001; Wu *et al*. 2003). It was further supported by the tomographic images showing that the Pacific ocean plate has ponded along the top of the mantle transition zone under the eastern NCC over 2000 km from the Japan trench (Zhu and Zheng 2009). Thus, it appears that Phanerozoic SCLM was added to most parts of eastern China along a NNE trend. This is consistent with the formation of the new lithosphere being related to the evolution of the Circum-Pacific continental margin during the Mesozoic and Cenozoic. We support this model because the present SCLM beneath the study area is virtually 'oceanic' in both mineral and bulk rock compositions. Therefore, the upwelling of asthenospheric mantle material by subduction of the Pacific oceanic plate seems to be the most reasonable interpretation for the thinning of ancient SCLM. The old T_{RD} ages, 1.0–1.9 Ga, in some mantle xenoliths from KD, LG, and WQ volcanic fields (Wu *et al*. 2003, 2007) are most likely due to a mixing of old SCLM and newly added asthenospheric material. Furthermore, no other geodynamic processes were active in the study area in the Mesozoic–Cenozoic period except for the west-dipping subduction of the Pacific ocean plate beneath the NCC since the early Mesozoic. The amalgamation of XMOB with NCC took place before, approximately at the end of Permian (Wu *et al*. 2011).

Possible processes controlling the oxidation states of mantle rocks

Tectonic setting and relations with fO_2

Previous studies on mantle rocks in various tectonic settings show that spinel-facies peridotites record fO_2 in a range of ΔFMQ ±2 log units with exceptionally high values in subarc mantle (Frost and McCammon 2008). The fO_2 range for a given geological setting is usually within 1 to 2 log units, indicating that it is heterogeneous in a small domian of mantle.

Upper mantle closely linked to the asthenosphere falls at the reduced end of this fO_2 range, whereas samples with long histories in the lithosphere or from subduction zones appear more oxidized (Frost and McCammon 2008). For example, abyssal peridotites as the residues of middle ocean ridge basalts (MORB) record the lowest fO_2 of spinel-facies peridotites (Bryndzia and Wood 1990); Peridotite massifs, such as Ronda in Spain and Beni Bousera in Morocco, are considered to represent protruded

asthenospheric mantle and record the comparable fO_2 values with abyssal peridotites (Wood *et al*. 1990). The SCLM xenoliths usually record slightly higher fO_2 than abyssal peridotites (Wood *et al*. 1990; Ionov and Wood 1992). It is generally considered that the oxidizing nature of SCLM is caused by adding of Fe^{3+}, CO_2, or carbonate to mantle (McGuire *et al*. 1991). Subduction setting records the highest fO_2 values and forms hydrous minerals (Wood and Virgo 1989; Brandon and Draper 1996). Although exact process are still under discussion, an undebatable fact is that the oxidized component is transferred from slabs to the overlying mantle through slab melt and fluids (Wood *et al*. 1990; Lécuyer and Ricard 1999). These oxidizing materials, such as Fe^{3+} and carbonate, from sediments and slabs may be incorporated into mantle wedges and oxidize the overlying mantle wedge (Mungall 2002; Hattori *et al*. 2005).

Old cratonic mantle contains both spinel-facies peridotites at shallow levels and garnet-facies peridotites at deeper levels. The values of fO_2 (Δ log fO_2 FMQ = –1.5 to –4.5) decreases with increasing depth owing to the effect of pressure on controlling Fe^{3+}/Fe^{2+} equilibria (Frost and McCammon 2008).

Partial melting and metasomatism

In the study area, underlying the old cratonic cover is a young lithospheric mantle that is made up with the asthenospheric material. This newly formed lithospheric mantle has undergone a low degree of partial melting after the mid-Mesozoic and minor metasomatism by subsequent silicate-melt.

The variable lithologies (lherzolite and harzburgite), a range of Cr# in Spl, and the evidence of metasomatism in our samples suggest that the redox state may have been influenced by partial melting in the new SCLM and the subsequent metasomatism during the generation of the Cenozoic volcanic fields.

Partial melting is considered to result in reduction of fO_2 in the residual mantle as Fe^{3+} is preferentially incorporated in partial melt (Canil *et al*. 1994). However, our Spl-facies lherzolite and harzburgite samples show very similar fO_2 values ranging from FMQ −2.64 to +0.39 with no correlation between fO_2 and Cr# of Spl (Figure 11), suggesting that partial melting was not accompanied by fO_2 changes. Our result is consistent with comparable fO_2 values between mid-oceanic ridge basalts and the abyssal peridotites (Bézos and Humler 2005). In addition, xenoliths from KD, LG, and CBS in the northeastern margin of NCC show fO_2 values similar to those from WQ and JL in the southern margin of XMOB, suggesting that the mantles beneath the joint area of NCC and XMOB are the same in nature.

Cryptic metasomatism by silicate melt may alter the redox state of mantle. Therefore, fO_2 values of these

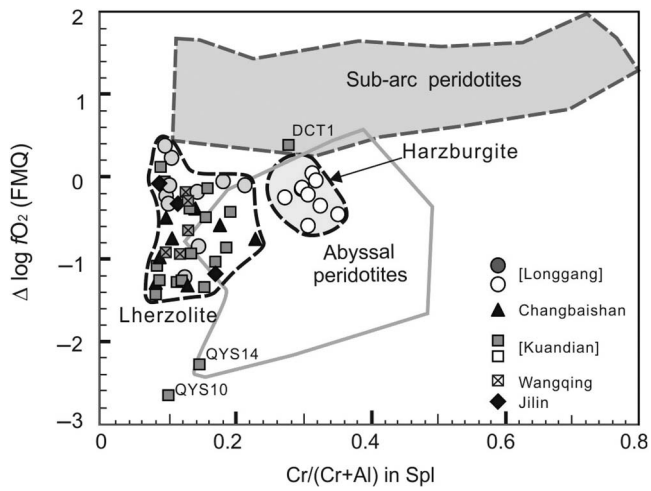

Figure 11. Values of fO_2 relative to FMQ buffer (ΔfO_2 (FMQ)) *versus* Cr# in spinel for peridotites from the northeast margin of NCC and southern margin of XMOB compared with abyssal peridotites (Bryndzia and Wood 1990) and sub-arc mantle peridotites compiled by Wang *et al*. (2008a). Data of Changbaishan are from Wang *et al*. (2012b). Symbols are the same as Figure 5.

samples likely reflect the imprint of the metasomatizing melt. However, samples (e.g. LQL7, LQL4, DLW5, DLW6, DYS5, HSW3, and DCT1) with clear evidence of metasomatism show fO_2 values ranging from FMQ –1.32 to +0.39, which are very similar to those of samples free of metasomatism. The evidence suggests that the infiltration of silicate melt did not alter fO_2 (Table 5). Alternatively, the metasomatic agent had similar fO_2 and therefore would not modify the peridotite during metasomatism. This is consistent with the proposal that the metasomatic agent from underlying asthenosphere mantle would have fO_2 slightly below the FMQ buffer. Therefore, it makes sense to consider the metasomatizing agent as co-genetic with the parental magmas of the host basalts in the area, that is, the metasomatizing melt together with those partial melt formed in response to the upwelling of asthenosphere in Cenozoic time. The presence of phlogopite and amphibole has been reported in mantle xenoliths from Cenozoic basalts in the EB of NCC, such as Jinlongdingzi and Hongqilinchang in LG, Nushan in Anhui, and Hannuoba in Hebei (Shi *et al*. 1999; Li and Wang 2002). The data suggest that the metasomatic agent was H_2O-rich melt with relatively low fO_2.

Most samples from this study plot within the graphite stability field at a wide range of equilibrium temperatures (740–1210°C; Figure 12). Theoretically, the samples are in equilibrium with CH_4-bearing fluids. Our interpretation is further supported by the compositions of fluid inclusions in some Cenozoic peridotites at Hannuoba, LG, WQ, and Jiaohe of the NCC. For example, Du *et al*. (1995) reported that some fluid inclusions in Spl-facies lherzolites from the above xenolith localities contain CH_4 up to 12.1–17.5 mole%. Therefore, it is not surprising to see

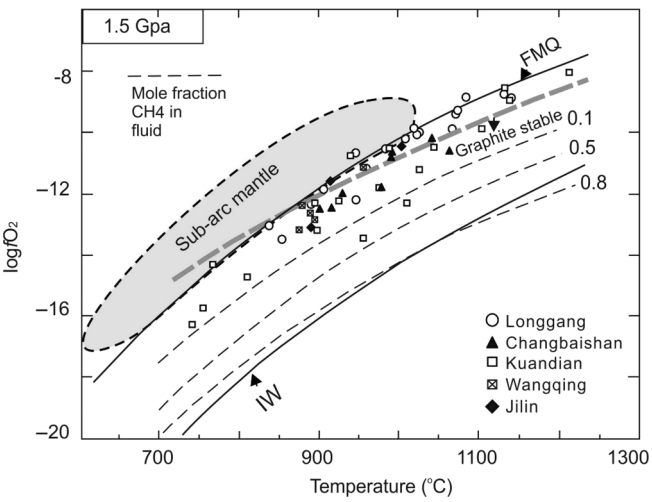

Figure 12. Mole fraction of CH_4 in C-H-O fluids on a diagram of fO_2 *versus* temperatures (modified after Wood *et al*. 1990). The values for mantle xenoliths from the northeast margin of NCC and southern margin of XMOB (this study) are compared to those from other sub-arc mantles compiled by Wang *et al*. (2007). Data of Changbaishan are from Wang *et al*. (2012b). IW, iron-wustite buffer. Note that most peridotites from the study area plot in the field of CH_4-bearing field.

that some metasomatized mantle samples have comparable fO_2 values with those anhydrous peridotites because the metasomatizing agent was reduced in oxidation state.

Our fO_2 data suggest that mantle xenoliths enclosed in Cenozoic basaltic rocks from the northeastern margin of NCC and southern margin of XMOB most likely represent the newly accreted SCLM formed from upwelling asthenosphere in the early to middle Mesozoic. The heat from the upwelling asthenosphere has likely contributed to partial melting of the newly formed SCLM and eruption of basaltic rocks. This partial melting resulted in minor, but varying degrees of depletion in the lherzolites and harzburgite. Since the amounts of melt are minor, the metasomatism in the new SCLM was also minor.

In summary, this study finds no evidence to support the proposal that partial melting results in the change of fO_2. Likewise, metasomatism is not necessarily accompanied by changes of fO_2 because it depends on the nature of the metasomatic agent, and various types of metasomatic agents are formed in different tectonic settings. We suggest that tectonic setting and geodynamic processes are the foundamental factors in controlling mantle fO_2.

Conclusions

Mantle xenoliths enclosed in Quaternary volcanic rocks in the KD, LG, CBS, WQ, and JL volcanic fields are Spl-facies lherzolites and harzburgites. Moderate values of Fo in Ol and low Cr# in Spl suggest that the xenoliths underwent a low degree of partial melting, 4–6%. Both bulk rock and mineral compositions of these samples are relatively fertile and similar to those of the oceanic mantle and asthenospheric mantle.

Our mantle peridotites show low degrees of minor metasomatism by spatially associated silicate melt. The calculated fO_2 values of lherzolites and harzburgites range from FMQ –2.64 to +0.39, comparable to the abyssal peridotites and peridotite massifs from Ronda in Spain and Beni Bousera in Morocco. Our data suggest that both partial melting and metasomatism were not accompanied by changes of fO_2.

Reduced oxidation state, bulk rock, and mineral compositions of our peridotites, together with previous results, suggest that the present-day lithospheric mantle beneath the northeastern margin of the NCC likely formed from an upwelling asthenospheric mantle triggered by the west-dipping subduction of the Pacific oceanic plate. Thus, our study supports that the refractory subcontinental keel was mostly replaced by a younger and more fertile lithospheric mantle in eastern China.

Acknowledgements

This work was financially supported by a grant from the National Natural Science Foundation of China (No. 41173034) to J. Wang and a grant from the Natural Science and Engineering Research Council of Canada to K. Hattori. This work was also supported by a grant from the China Geological Survey (No. 1212011121088). We thank Smita Mohanty and Nimal DeSilva for the chemical analysis of samples at the University of Ottawa, and S. Zheng and Z.-C. Hu at China University of Geosciences in Wuhan for their technical support during the electron microprobe and LA-ICP-MS analyses. We also thank Q.-F. Yang for his help in the field work. The manuscript benefited from the constructive comments of Jeffrey Hedenquist.

References

Arai, S., 1994, Characterization of spinel peridotites by olivine-spinel compositional relationships: Review and interpretation: Chemical Geology, v. 111, p. 191–204.

Arai, S., and Ishimaru, S., 2008, Insights into petrological characteristics of the lithosphere of mantle wedge beneath Arcs through peridotite xenoliths: A review: Journal of Petrology, v. 49, p. 665–695.

Arai, S., Ishimaru, S., and Okrugin, V.M.., 2003, Metasomatized harzburgite xenoliths from Avacha volcano as fragments of mantle wedge of the Kamchatka arc: Implication for the metasomatic agent: The Island Arc, v. 12, p. 233–246.

Ballhaus, C., 1993, Redox states of lithospheric and asthenospheric upper mantle: Contributions to Mineralogy and Petrology, v. 114, p. 331–348.

Ballhaus, C., Berry, R.F., and Green, D.H., 1991, High pressure experimental calibration of the olivine-orthopyroxene-spinel oxygen geobarometer: Implications for the oxidation state of the upper mantle: Contributions to Mineralogy and Petrology, v. 107, p. 27–40.

Ballhaus, C., and Frost, B.R., 1994, The generation of oxidized CO_2-bearing basaltic melts from reduced CH4-bearing upper

mantle sources: Geochimica et Cosmochimica Acta, v. 58, p. 4431–4440.

Bell, D.R., Gregoire, M., Grove, T.L., Chatterjee, N., Carlson, R.W., and Buseck, P.R., 2005, Silica and volatile-element metasomatism of Archean mantle: A xenolith-scale example from the Kaapvaal Craton: Contributions to Mineralogy and Petrology, v. 150, p. 251–267.

Bézos, A., and Humler, E., 2005, The $Fe^{3+}/\Sigma Fe$ ratios of MORB glasses and their implications for mantle melting: Geochimica et Cosmochimica Acta, v. 69, p. 711–725.

Bodinier, J.L., Menzies, M.A., Shimizu, N., Frey, F.A., and McPherson, E., 2004, Hydrous, silicate and carbonate metasomatism at Lherz, France: Contemporaneous derivatives of silicate melt–harzburgite reaction: Journal of Petrology, v. 45, p. 299–320.

Brandon, A.D., and Draper, D.S., 1996, Constraints on the origin of the oxidation state of mantle overlying subduction zones: An example from Simcoe, Washington, USA: Geochimica et Cosmochimica Acta, v. 60, p. 1739–1749.

Brey, G.P., and Köhler, T., 1990, Geothermobarometry in four-phase lherzolites: II. New thermobarometers, and practical assessment of existing thermobarometers: Journal of Petrology, v. 31, p. 1353–1378.

Bryndzia, L.T., and Wood, B.J., 1990, Oxygen thermobarometry of abyssal spinel peridotites: The redox state and C-O-H volatile composition of the Earth's suboceanic mantle: American Journal of Sciences, v. 290, p. 1093–1116.

Canil, D., O'Neill, H., St, C., Pearson, D.G., Rudnick, R.L., and McDonough, W.F., 1994, Ferric iron in peridotites and mantle oxidation states: Earth and Planetary Science Letters, v. 123, p. 205–220.

Cerighton, S., Stachel, T., Eichenberg, D., and Luth, R.W., 2010, Oxidation state of the lithospheric mantle beneath Diavik diamond mine, central Slave Craton, NWT, Canada: Contributions to Mineralogy and Petrology, v. 159, p. 645–657.

Coltorti, M., Bonadiman, C., Hinton, R.W., Siena, F., and Upton, B.G., 1999, Carbonatite metasomatism of the oceanic upper mantle: Evidence from clinopyroxenes and glasses in ultramafic xenoliths of Grande Comore, Indian Ocean: Journal of Petrology, v. 40, p. 133–165.

Daniels, L.R.M., and Gurney, J.J., 1991, Oxygen fugacity constraints on the southern African lithosphere: Contributions to Mineralogy and Petrology, v. 108, p. 154–161.

DeHoog, J.C.M., Hattori, K.H., and Hoblitt, R.P., 2004, Oxidized sulfur-rich mafic magma at Mount Pinatubo, Philippines: Contributions to Mineralogy and Petrology, v. 146, p. 750–761.

Deng, J.F., Su, S.Y., Niu, Y.L., Liu, C., Zhao, G.C., Zhao, X.G., Zhou, S., and Wu, Z.X., 2007, A possible model for the lithospheric thinning of North China Craton: Evidence from the Yanshanian (Jura-Cretaceous) magmatism and tectonism: Lithos, v. 96, p. 22–35.

Dick, J.J.B., and Bullen, T., 1984, Chromian spinel as a petrogenetic indicator in abyssal and alpine-type peridotites and spatially associated lavas: Contributions to Mineralogy and Petrology, v. 86, p. 54–76.

Du, L.T., Wang, J., and Huang, S.T., 1995, Release of hydrocarbons from the Earth: Bulletion of mineralogy: Petrology and Geochemistry, v. 1, p. 45–47 (in Chinese with English abstract).

Fan, W.M., Zhang, H.F., Baker, J., Jarvis, K.E., Mason, P.R.D., and Menzies, M.A., 2000, On and off the North China Craton: Where is the Archean keel?: Journal of Petrology, v. 41, p. 933–950.

Frost, D.J., and McCammon, C.A., 2008, The redox state of Earth's mantle: Annual Review of Earth and Planetary Sciences, v. 36, p. 389–420.

Gao, S., Rudnick, R.L., Carlson, R.W., McDonough, W.F., and Liu, Y.S., 2002, Re–Os evidence for replacement of ancient mantle lithosphere beneath the North China Craton: Earth and Planetary Science Letters, v. 198, p. 307–322.

Gao, S., Rudnick, R.L., Yuan, H.L., Liu, X.M., Liu, Y.S., Xu, W.L., Ling, W.L., Ayers, J., Wang, X.C., and Wang, Q.H., 2004, Recycling lower continental crust in the North China Craton: Nature, v. 432, p. 892–897.

Griffin, W.L., and O'Reilly, S.Y., 2007, Cratonic lithospheric mantle: Is anything subducted?: Episodes, v. 30, p. 43–53.

Gueddari, K., Piboule, M., and Amossé, J., 1996, Differentiation of platinum-group elements (PGE) and of gold during partial melting of peridotites in the lherzolitic massifs of the Betico-Rifean range (Ronda and Beni Bousera): Chemical Geology, v. 134, p. 181–197.

Hattori, K.H., and Keith, J.D., 2001, Contribution of mafic melt for porphyry deposits: Evidence from Pinatubo and Bingham: Mineralium Deposita, v. 36, p. 799–806.

Hattori, K.H., Takahashi, Y., Guillot, S., and Johanson, B., 2005, Occurrence of arsenic (V) in forearc mantle serpentinites based on X-ray absorption spectroscopy study: Geochimica et Cosmochimica Acta, v. 69, p. 5585–5596.

Hattori, K.H., Wallis, S., Enami, T., and Mizukami, T., 2010, Subduction of mantle wedge peridotites: Evidence from the Higashi-akaishi ultramafic body in the Sanbagawa metamorphic belt: Island Arc, v. 19, p. 192–207.

Ionov, D.A., and Wood, B.J., 1992, The oxidation state of subcontinental mantle: Oxygen thermobarometry of mantle xenoliths from central Asia: Contributions to Mineralogy and Petrology, v. 111, p. 179–193.

Johnson, K.T.M., Dick, H.J.B., and Shimizu, N., 1990, Melting in the oceanic upper mantle: An ion microprobe study of diopside in abyssal peridotites: Journal of Geophysical Research, v. 95, p. 2661–2678.

Kelemen, P.B., Hart, S.R., and Bernstein, S., 1998, Silica enrichment in the continental upper mantle via melt/rock reaction: Earth and Planetary Science Letters, v. 164, p. 387–406.

Kuritani, T., Kimura, J.-I., Miyamoto, T., Wei, H.Q., Shimano, T., Maeno, F., Jin, X., and Taniguchi, H., 2009, Intraplate magmatism related to deceleration of upwelling asthenospheric mantle: Implications from the Changbaishan shield basalts, northeast China: Lithos, v. 112, p. 247–258.

Kusky, T.M., Windley, B.F., and Zhai, M.G.. 2007, Lithospheric thinning in eastern Asia: Constraints, evolution, and tests of models: Geological Society, London, Special publications, v. 280, p. 331–343.

Lécuyer, C., and Ricard, Y., 1999, Long-term fluxes and budget of ferric iron: Implication for the redox states of the Earth's mantle and atmosphere: Earth and Planetary Science Letters, v. 165, p. 197–211.

Li, J.P., and Wang, J., 2002, Mantle redox state evolution in eastern China and its implications: Acta Geologica Sinica, v. 76, p. 238–248.

Liu, J., Han, J., and Fyfe, W.S., 2001a, Cenozoic episodic volcanism and continental rifting in northeast China and possible link to Japan Sea development as revealed from K-Ar geochronology: Tectonophysics, v. 339, p. 385–401.

Liu, Y.S., Gao, S., and Jin, S.Y., 2001b, Geochemistry of lower crustal xenoliths from Neogene Hannuoba basalt, North China Craton: Implications for petrogenesis and lower crustal composition: Geochimica et Cosmochimica Acta, v. 65, p. 2589–2604.

Lu, F.X., Molan, E., and Deng, J.F., 1983, Ultramafic inclusions and megacrysts in alkaline basalts from Huangyishan, Kuandian, Liaoning Provinces, China: Petrological Research, v. 3, p. 77–88 (in Chinese with English abstract).

McCammon, C., and Kopylova, M.G., 2004, A redox profile of the Slave mantle and oxygen fugacity control in the cratonic mantle: Contributions to Mineralogy and Petrology, v. 14, p. 55–68.

McCammon, C.A., Griffin, W.L., Shee, S.H., O'Neill, H., and St, C., 2001, Oxidation during metasomatism in ultramafic xenoliths from the Wesselton kimberlite, South Africa: Implications for the survival of diamond: Contributions to Mineralogy and Petrology, v. 141, p. 287–296.

McDonough, W.F., and Sun, S.S., 1995, The composition of the Earth: Chemical Geology, v. 120, p. 223–253.

McGuire, A.V., Dyar, M.D., and Nielson, J., 1991, Metasomatic oxidation of upper mantle peridotite: Contributions to Mineralogy and Petrology, v. 109, p. 252–264.

McInnes, B.I.A., Gregoire, M., Binns, R.A., Herzig, P.M., and Hannington, M.D., 2001, Hydrous metasomatism of oceanic subarc mantle, Lihir, Papua New Guinea: Petrology and geochemistry of fluid-metasomatised mantle wedge xenoliths: Earth and Planetary Science Letters, v. 88, p. 169–183.

Mungall, J.E., 2002, Roasting the mantle: Slab melting and the genesis of major Au and Au-rich Cu deposits: Geology, v. 30, p. 915–918.

Nell, J., and Wood, B.J., 1991, High-temperature electrical measurements and thermodynamic properties of Fe_3O_4-$FeCr_2O_4$-$MgCr_2O_4$-$FeAl_2O_4$ spinels: American Mineralogist, v. 76, p. 405–426.

Niu, Y., 2005, Generation and evolution of basaltic magmas: Some basic concepts and a new view on the origin of Mesozoic–Cenozoic basaltic volcanism in Eastern China: Geological Journal of China Universities, v. 11, no. 1, p. 9–46.

Norman, M.D., 1998, Melting and metasomatism in the continental lithosphere: Laser ablation ICPMS analysis of minerals in spinel lherzolites from eastern Australia: Contributions to Mineralogy and Petrology, v. 130, p. 240–255.

Parkinson, I.J., and Arculus, R.J., 1999, The redox state of subduction zones: Insights from arc-peridotites: Chemical Geology, v. 160, p. 409–423.

Parkinson, I.J., Arculus, R.J., and Eggins, S.M., 2003, Peridotite xenoliths from Grenada, Lesser Antilles Island Arc: Contributions to Mineralogy and Petrology, v. 146, p. 241–262.

Qi, Q., Taylor, L.A., and Zhou, X.M., 1995, Petrology and geochemistry of mantle peridotite xenoliths from SE China: Journal of Petrology, v. 36, p. 55–79.

Shi, L.B., Lin, C.Y., Han, X.L., and Chen, X.D., 1999, Principal features of mantle xenoliths in Jinlongdingzi volcanics, Longgang volcano cluster, Jilin Province and their geological implications: Geological Review, v. 45, p. 308–318 (in Chinese with English abstract).

Smith, D., Riter, J.C.A., and Mertzman, S.A., 1999, Water–rock interactions, orthopyroxene growth and Si-enrichment in the mantle: Evidence in xenoliths from the Colorado Plateau, southwestern United States: Earth and Planetary Science Letters, v. 165, p. 45–54.

Wang, J., Hattori, K.H., Kilian, R., and Stern, C.R., 2007, Metasomatism of sub-arc mantle peridotites below southernmost South America: Reduction of fO_2 by slab-melt: Contributions to Mineralogy and Petrology, v. 153, p. 607–624.

Wang, J., Hattori, K.H., Li, J.-P., and Stern, C.R., 2008a, Oxidation state of Paleozoic subcontinental lithospheric mantle below the Pali Aike volcanic field in southernmost Patagonia: Lithos, v. 105, p. 98–110.

Wang, J., Hattori, K.H., and Stern, C.R., 2008b, Metasomatic origin of garnet orthopyroxenites in the subcontinental lithospheric mantle underlying Pali Aike volcanic field, southern South America: Mineralogy and Petrology, v. 94, p. 243–258.

Wang, J., Hattori, K.H., Xu, W.L., Yang, Y.Q., Xie, Z.P., Liu, J.L., and Song, Y., 2012a, Origin of ultramafic xenoliths in high-Mg diorites from east-central China based on their oxidation state and abundance of platinum group elements: International Geology Review, v. 54, p. 1203–1218.

Wang, J., Liu, J.L., Hattori, K.H., Xu, W.L., Xie, Z.P., and Song, Y., 2012b, Behavior of siderophile and chalcophile elements in the subcontinental lithospheric mantle beneath the Changbaishan Volcano, NE China: Acta Geologica Sinica, v. 86, p. 407–422.

Wang, Y., Li, C.F., Wei, H.Q., and Shan, X.J., 2003, Late Pliocene–recent tectonic setting for the Tianchi volcanic zone, Changbai Mountains, northeast China: Journal of Asian Earth Sciences, v. 21, p. 1159–1170.

Wei, H.Q., Wang, Y., Jin, J.Y., Gao, L., Yun, S.-H., and Jin, B.L., 2007, Timescale and evolution of the intracontinental Tianchi volcanic shield and ignimbrite-forming eruption, Changbaishan, NE China: Lithos, v. 96, p. 315–324.

Wells, P.R.A., 1977, Pyroxene thermometry in simple and complex systems: Contributions to Mineralogy and Petrology, v. 62, p. 119–139.

Wilde, S.A., and Zhao, G.C., 2005, Archean to Paleoproterozoic evolution of the North China Craton: Journal of Asian Earth Sciences, v. 24, p. 519–522.

Windley, B.F., Xiao, W.J., and Maruyama, S.. 2011, Thinning/delamination of sub-continental lithospheric mantle under eastern China: The role of water and multiple subduction: International Conferences on Craton Formation and Destruction, Beijing, Abstract, p. 21.

Wood, B.J., Bryndzia, L.T., and Johnson, K.E., 1990, Mantle oxidation state and its relationship to tectonic environment and fluid speciation: Science, v. 248, p. 337–345.

Wood, B.J., and Virgo, D., 1989, Upper mantle oxidation state: Ferric iron content of lherzolite spinels by ^{57}Fe Mössbauer pectroscopy and resultant oxygen fugacities: Geochimica et Cosmochimica Acta, v. 53, p. 1277–1291.

Woodland, A.B., and Koch, M., 2003, Variation in oxygen fugacity with depth in the upper mantle beneath the Kaapvaal Craton, southern Africa: Earth and Planetary Science Letters, v. 214, p. 295–310.

Woodland, A.B., Kornprobst, J., and Tabit, A., 2006, Ferric iron in orogenic lherzolite massifs and controls of oxygen fugacity in the upper mantle: Lithos, v. 89, p. 222–241.

Woodland, A.B., Kornprobst, J., and Wood, B.J., 1992, Oxygen thermobarometry of orogenic lherzolite massifs: Journal of Petrology, v. 33, p. 203–230.

Wu, F.Y., Sun, D.Y., Ge, W.C., Zhang, Y.B., Grant, M.L., Wilde, S.A., and Jahn, B.M., 2011, Geochronology of the Phanerozoic granitoids in northeastern China: Journal of Asian Earth Sciences, v. 41, p. 1–30.

Wu, F.Y., Walker, R.J., Ren, X.W., Sun, D.Y., and Zhou, X.H., 2003, Osimium isotopic constraints on the age of lithospheric mantle beneath northeastern China: Chemical Geology, v. 196, p. 107–129.

Wu, F.Y., Yang, J.H., Chu, Z.Y., Xie, L.W., Yang, Y.H., and Li, Q.L., 2007, Dating the subcontinental lithospheric mantle: Earth Science Frontiers, v. 14, p. 76–86 (in Chinese with English abstract).

Xiao, W.J., Windley, B.F., Hao, J., and Zhai, M.G., 2003, Accretion leading to collision and the Permian Solonker suture, Inner Mongolia, China: Termination of the Central Asian orogenic belt: Tectonics, v. 22, p. 1069. doi: 10.1029/2002 TC001484.

Xu, Y.G., 2001, Thermo-tectonic destruction of the Archean lithospheric keel beneath eastern China: Evidence, timing and mechanism: Physics and Chemistry of the Earth, v. 26A, p. 747–757.

Xu, Y.G., Zhang, H.H., Song, S.Y., Qin, X.F., Kuang, Y.S., and Hong, L.B., 2011, Pacific subduction as a trigger of the destruction of the North China Craton: A petrologic-geochemical perspective: International Conferences on Craton Formation and Destruction, Beijing, Abstract, p. 21.

Yang, J.H., Wu, F.Y., and Wilde, S.A., 2003, Geodynamic setting of large-scale Late Mesozoic gold mineralization in the North China Craton: An association with lithospheric thinning: Ore Geology Reviews, v. 23, p. 125–152.

Yaxley, G.M., Green, D.H., and Kamenetsky, V., 1998, Carbonatite metasomatism in the southeastern Australia lithosphere: Journal of Petrology, v. 39, p. 1917–1930.

Zhang, J., Zhao, G.C., Li, S.Z., Sun, M., Liu, S.W., Wilde, S.A., Kroner, A., and Yin, C.Q., 2007, Deformation history of the Hengshan Complex: Implications for the tectonic evolution of the Trans-North China Orogen: Journal of Structural Geology, v. 29, p. 933–949.

Zhang, J., Zhao, G.C., Sun, M., Wilde, S.A., Li, S.Z., and Liu, S.W., 2006, High-pressure mafic granulites in the Trans-North China Orogen: Tectonic significance and age: Gondwana Research, v. 9, p. 349–362.

Zhao, G.C., Sun, M., Wilde, S.A., and Li, S.Z., 2005, Late Archean to Paleoproterozoic evolution of the North China Craton: Key issues revisited: Precambrian Research, v. 136, p. 177–202.

Zheng, J.P., Griffin, W.L., O'Reilly, S.Y., Yang, J.S., Li, T.F., Zhang, M., Zhang, R.Y., and Liou, J.G., 2006, Mineral chemistry of peridotites from Paleozoic, Mesozoic and Cenozoic lithosphere: Constraints on mantle evolution beneath eastern China: Journal of Petrology, v. 46, p. 2233–2256.

Zheng, J.P., Sun, M., Zhou, M.F., and Robinson, P., 2005, Trace elemental and PGE geochemical constraints of Mesozoic peridotitic xenoliths on lithospheric evolution of the North China Craton: Geochimica et Cosmochimica Acta, v. 69, p. 3401–3418.

Zhi, X.C., Peng, Z.C., Chen, D.G., Yu, C.J., Sun, W.D., and Reisberg, L., 2001, The longevity of subcontinental lithospheric mantle beneath Jiangsu-Anhui region: Science in China, Series D, v. 44, p. 1110–1118.

Zhu, R.X., and Zheng, T.Y., 2009, Destruction geodynamics of the North China Craton and its Paleoproterozoic plate tectonics: Chinese Science Bulletin, v. 54, p. 3354–3366.